

Molecular determinants for the association of human hormone-sensitive lipase with lipid droplets

Received: 27 June 2024

Accepted: 2 April 2025

Published online: 12 April 2025



Han Peng^{1,2,3,7}, Qikui Xu^{3,4,7}, Ting Zhang^{2,3}, Jiakai Zhu^{2,3}, Jinheng Pan^{2,5}, Xiaoyu Guan^{2,3}, Shan Feng^{2,5}, Jianping Wu^{2,5}  & Qi Hu^{2,4,6} 

Lipid droplets (LDs) are the main cellular storage sites for triacylglycerols (TAGs), playing an important role in energy homeostasis and cell signaling. Hydrolysis of the stored TAGs begins with conversion of TAGs into diacylglycerols (DAGs) by adipose triglyceride lipase (ATGL), followed by hydrolysis of DAGs by hormone-sensitive lipase (HSL). Despite the central role of HSL in lipolysis, the molecular determinants for its LD association have remained elusive. Here, we report the cryo-EM structure of human HSL at 3.4 Å. Combining this with hydrogen-deuterium exchange mass spectrometry, biochemical and cellular assays, we identify residues 489–538, referred to as the “H-motif”, and the N-terminal 4-helix bundle of HSL as LD-binding motifs mediating direct interaction of HSL with LDs. LD binding mediated by the LD-binding motifs is independent of HSL phosphorylation catalyzed by the cAMP-dependent kinase PKA. Our findings provide insight into the LD binding mechanism of HSL, advancing our understanding of the regulation of lipolysis.

Lipid droplets (LDs) are organelles found in most cell types, serving as the primary storage sites for neutral lipids such as triacylglycerols (TAGs) and sterol esters (SEs)^{1,2}. LDs have a distinctive structure comprising a core of neutral lipids surrounded by a phospholipid monolayer, which differs from the bilayer of other organelles^{1,2}. LDs play a crucial role in cellular energy metabolism and lipid homeostasis². Furthermore, LDs interact with other cellular components, influencing processes like cell signaling and membrane trafficking².

The TAGs in LDs are broken down into free fatty acids (FFAs) and glycerol during periods of energy demand³. This process, known as lipolysis, is sequentially catalyzed by three neutral lipases, including adipose triglyceride lipase (ATGL) for hydrolyzing a TAG into diacylglycerols (DAG) and an FFA, hormone-sensitive lipase (HSL) for hydrolyzing a DAG into monoglycerides (MAG) and an FFA, and

monoglyceride lipase (MGL) for hydrolyzing a MAG into glycerol and an FFA³.

HSL was identified together with MGL in 1964 in a study of lipase activities in rat and rabbit adipose tissues⁴. HSL was named because its activity can be stimulated by hormones such as norepinephrine and epinephrine⁴. Since then, a key question is how HSL senses hormones. Much of what we know about the regulation of HSL comes from studies of rat HSL. Hormones can activate protein kinase A (PKA), which is a cAMP-dependent kinase, through the GPCR-Gas-adenylyl cyclase-cAMP-PKA pathway^{5–9}. The activated PKA catalyzes the phosphorylation of rat HSL at S563, S659, and S660 (refs. 10,11), corresponding to S552, S649, and S650 in human HSL, respectively. Phosphorylation by PKA can increase the enzyme activity of HSL in cell lysates¹¹, which could be explained by directly activating HSL and indirectly activating HSL by promoting the association of HSL with LDs^{12–14}.

¹College of Life Sciences, Zhejiang University, Hangzhou, Zhejiang, China. ²School of Life Sciences, Westlake University, Hangzhou, Zhejiang, China.

³Westlake Laboratory of Life Sciences and Biomedicine, Hangzhou, Zhejiang, China. ⁴Key Laboratory of Structural Biology of Zhejiang Province, School of Life Sciences, Westlake University, Hangzhou, Zhejiang, China. ⁵Mass Spectrometry & Metabolomics Core Facility, Biomedical Research Center, Westlake University, Hangzhou, Zhejiang, China. ⁶Institute of Biology, Westlake Institute for Advanced Study, Hangzhou, Zhejiang, China. ⁷These authors contributed equally: Han Peng, Qikui Xu. ✉e-mail: wujianping@westlake.edu.cn; huqi@westlake.edu.cn

Activated PKA is also known to catalyze the phosphorylation of other LD-related proteins, including perilipin 1 (PLIN1)^{15–17}, perilipin 5 (PLIN5)¹⁸, ATGL¹⁹, and CGI-58 (also called ABHD5)²⁰. PLIN1 is a scaffold protein on LDs and is involved in the recruitment of HSL to LDs²¹. Sztalryd et al. reported that phosphorylation at three serine residues at the N-terminal region of PLIN1 is essential for the recruitment of HSL to LDs in nonadipocyte CHO (Chinese hamster ovary) cells²², but Miyoshi et al. demonstrated that PLIN1 mediates the translocation of HSL to LDs independently of PLIN1 phosphorylation in MEF (murine embryonic fibroblasts) adipocytes¹⁵. The controversial conclusions regarding the role of PLIN1 phosphorylation in the recruitment of HSL to LDs may be due to different cell lines that were used in the two studies. However, both studies suggest an important role of PLIN1 in the regulation of LD binding of HSL.

It has been reported that without hormone stimulation, HSL can already bind to LDs, with the binding ratio varying in different studies. In adipocytes from young male rats, the LD binding ratio increased from about 40% to 80% after isoproterenol stimulation; but in mature male rats, the ratio remained less than 20% regardless of isoproterenol stimulation²³. Another study also reported that in adipocytes from young male rats, the LD-binding ratio of HSL increased from 60% to 80% after being stimulated with various hormones²⁴. Inside the rat muscle fiber, the binding ratio increased from 30% to 42% after epinephrine stimulation and further increased to 59% after muscle contraction²⁵. These studies provided evidence that HSL associates with LDs in its basal state, and the association can be further stimulated by hormones in a context-dependent manner. However, the molecular basis for the association of HSL with LDs is unclear.

In this study, we find that HSL can directly associate with LDs through a short sequence in its regulatory domain and a 4-helix bundle in its N-terminal domain. We determine the cryo-electron microscopy (cryo-EM) structure of human HSL at 3.4 Å resolution and analyze the structural changes induced by LDs binding using hydrogen-deuterium exchange mass spectrometry (HDX-MS). Using an *in vitro* reconstituted artificial lipid droplet (ALD) binding assay and a cellular imaging assay, we find that the regulatory domain (residues 489–659) of HSL is essential to its LD-binding ability. We then narrow down the LD-binding sequence to residues 489 to 538 and define this sequence as the “H-motif”. Deletion or mutations of the H-motif decrease the enzymatic activity of HSL towards a long acyl chain substrate but have no influence on the hydrolysis of pNPB, a short acyl chain substrate. Additionally, we identify a 4-helix bundle (residues 1–136) in the N-terminal domain of HSL as another LD-binding motif in HSL.

We further investigate the importance of the LD-binding motifs in the context of PKA activation in both 3T3-L1 preadipocytes and adipocytes. Our results demonstrate that forskolin-induced PKA activation increases HSL phosphorylation levels independently of the LD-binding status of HSL. The LD-binding motifs are essential for HSL binding to LDs, regardless of PKA activation. Notably, PKA-catalyzed phosphorylation of HSL does not affect its LD-binding ability in 3T3-L1 preadipocytes but enhances HSL localization to LDs in 3T3-L1 adipocytes. These findings suggest that, in addition to interactions mediated by the LD-binding motifs, which are independent of PKA-catalyzed phosphorylation, HSL localizes to LDs also through PKA-dependent interactions in 3T3-L1 adipocytes. Additionally, we find that phosphorylation has no impact on the enzymatic activity or LD-binding ability of purified HSL, indicating that PKA may not directly modulate HSL's enzymatic activity or LD binding but may indirectly facilitate HSL localization to LDs in 3T3-L1 adipocytes.

Results

HSL interacts with artificial lipid droplets

HSL has three major isoforms: HSLtes, HSLbeta, and HSLadi, which are expressed in the testis²⁶, insulin-secreting β -cells²⁷, and adipocytes^{28,29}, respectively. The HSL in our study refers to the adipocyte isoform of

human HSL (UniProt: Q05469-2), which contains only residues 302–1076 of the testis isoform.

We overexpressed human HSL, which contains an N-terminal domain, a catalytic domain, and a regulatory domain inserted in the catalytic domain (Fig. 1a), in Expi293F cells and purified it to homogeneity (Fig. 1b). The enzyme activity of the purified HSL was first evaluated using *p*-nitrophenyl butyrate (pNPB) as the substrate³⁰. The K_m and k_{cat} are 186.1 μ M and 124.5 s^{−1}, respectively (Fig. 1c). HSL lost its activity when its catalytic residue S424 was mutated to alanine (Fig. 1c). The enzyme activity of HSL was also evaluated using the EnzChek lipase substrate (Invitrogen), which is a fluorogenic analog of TAG. Only the wild-type (WT) HSL, but not the S424A mutant, hydrolyzed the EnzChek lipase substrate (Fig. 1d). These results confirm that the purified HSL is functional.

Next, we evaluated the LD-binding ability of HSL using a flotation assay³¹. We prepared artificial lipid droplets (ALDs) by mixing 1,2-dioleoyl-sn-glycero-3-phosphocholine (DOPC) with TAG following a method reported previously^{32,33}. Since the phospholipid monolayer of mammalian LDs mainly consists of phosphatidylcholine (PC) and phosphatidylethanolamine (PE) with a molar ratio of around 3:1 (ref. 34), we also prepared ALDs by mixing DOPC and 1,2-dioleoyl-sn-glycero-3-phosphoethanolamine (DOPE) (DOPC:DOPE = 3:1) with TAG (Fig. 1e). We first incubated the purified HSL with ALDs or the same volume of an assay buffer, then separated the ALD-bound HSL from unbound HSL using sucrose gradient centrifugation (Fig. 1f). After centrifugation, we collected three fractions named top, middle and bottom fractions. ALDs were enriched in the top fraction (Fig. 1f). In the absence of ALDs, HSL was mainly in the bottom fraction, while in the presence of ALDs, HSL was mainly in the top fraction (Fig. 1g). As a control, a soluble protein maltose-binding protein (MBP) was mainly in the bottom fraction no matter in the absence or presence of ALDs (Fig. 1g). We qualified HSL in the top fraction under different conditions and found that in the presence of ALDs prepared using the DOPC and DOPE mixture, about 80% of HSL was in the top fraction. In contrast, under the same conditions, less than 10% of MBP was in the top fraction (Fig. 1h). These results demonstrate that HSL can directly bind to ALDs. This finding is consistent with a previous report that HSL purified from rat adipose tissue can be incorporated into phosphatidylcholine vesicles³⁵.

Cryo-EM structure of human HSL

To understand how HSL binds to LDs, we attempted to solve the cryo-EM structure of HSL bound to ALDs but were unsuccessful. Instead, we solved the cryo-EM structure of HSL in the absence of ALDs. Before preparing the cryo-EM samples, we incubated HSL with HSL-IN-1, an inhibitor of HSL³⁶. The cryo-EM map has an overall resolution of 3.4 Å (Supplementary Table 1; Supplementary Figs. 1 & 2). The N-terminal domain and the catalytic domain were resolved in the cryo-EM map, while the majority of the regulatory domain (residues 492–637) was unresolved (Fig. 2a, b). The HSL inhibitor HSL-IN-1 was not observed in the cryo-EM map. The cryo-EM structure reveals a homodimeric state of HSL (Fig. 2b). Based on the homodimeric structure, the N-terminal domain is defined as residues 1–174, which contains a 4-helix bundle (residues 1–136). The catalytic domain is divided into three subdomains: CD1, consisting of residues 175–262; CD2, consisting of residues 263–488; and CD3, consisting of residues 660–775 (Fig. 2a, b).

The N-terminal 4-helix bundle from one HSL protomer contacts with the CD2 subdomain from the other protomer at the dimer interface (Fig. 2c). In addition, the CD1 subdomains from the two HSL protomers (Fig. 2d) also contact with each other at the dimer interface. The residues between N198 and R214 in CD1 were not resolved in the cryo-EM map.

Several crystal structures of bacterial homologs of human HSL have been reported^{37–41}. These bacterial homologs share a conserved catalytic domain. Unlike human HSL, they do not contain the

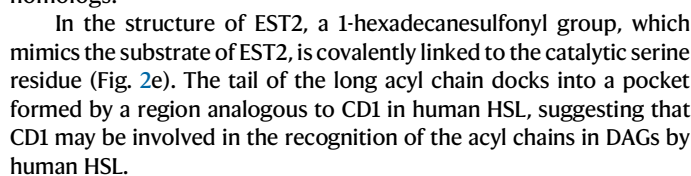


Fig. 1 | Characterization of purified human HSL. **a** The linear diagram of human HSL. **b** Size exclusion chromatography (SEC) of human HSL with a C-terminal FLAG tag. The FLAG-tagged HSL transiently expressed in Expi293F cells was firstly purified by anti-FLAG tag affinity resins, then further purified by an SEC column (Superdex 200 Increase). The peak fractions were analyzed by SDS-PAGE and visualized by Coomassie blue staining. The asterisk indicates a contaminant that was supposed to be a chaperone. We purified HSL several times, and the data in **b** represent the results of one such purification. **c, d** The enzymatic activity of the purified HSL was evaluated using pNPB (**c**) or the EnzChek lipase substrate (**d**) as the substrate of HSL, respectively (see methods). **e** Illustration of artificial lipid droplets (ALDs) preparation. ALDs were prepared by mixing phospholipids (DOPC/DOPE) with neutral lipids triacylglycerol (TAG). Created in BioRender. Hu, Q. (2025) <https://BioRender.com/t74d619>. **f** Illustration of the flotation assay. HSL or the control protein MBP was incubated with ALDs for 1 h at room temperature, and

then separated by sucrose gradient centrifugation. After centrifugation, the mixture was divided into three fractions, including the bottom (280 μ L), middle (260 μ L), and top (100 μ L) fractions. The ALDs were in the top fraction. **g** Evaluation of the proteins in the three fractions from the sucrose gradient centrifugation by SDS-PAGE followed by Coomassie blue staining. T, M, and B indicate the Top, middle, and bottom fractions, respectively. For each fraction, 20 μ L of the sample was loaded on the SDS-PAGE gel. The gels in **g** are the results of a representative experiment out of three independent experiments. The asterisk indicates a contaminant that was supposed to be HSP70. **h** Quantification of the percentages of HSL and MBP in the top fractions. HSL or MBP was incubated with the assay buffer (no ALDs), or with ALDs prepared with DOPC (100%) or a mixture of DOPC (75%) and DOPE (25%), and then separated by sucrose gradient centrifugation. The data in **c, d**, and **h** represent the mean \pm SD of three independent measurements. Source data are provided as a Source Data Fig. 1 file.

The regulatory domain is the dominant LD-binding region in HSL

In the cryo-EM structure, three internal regions, including residues 199–213, 325–336, and the regulatory domain (residues 489–659), are largely invisible, probably due to their inherent flexibility. To understand the roles of these regions in the LD-binding ability and enzymatic activity of HSL, we engineered HSL variants in which these regions were deleted and subsequently overexpressed in Expi293F cells. We successfully purified two variants, namely HSL(Δ 325–333) and HSL(Δ 489–659), where residues 325–333 and residues 489–659 were deleted, respectively. We also purified a variant, HSL($\Delta\Delta$), which had both residues 325–333 and residues 489–659 deleted. However, we failed to obtain well-behaved HSL with residues 198–214 deleted.

We evaluated whether these HSL variants can still bind to the ALDs using the flotation assay (Fig. 3a). Deletion of residues 325–333 only slightly decreased the binding of HSL to ALDs; in contrast, deletion of residues 489–659 significantly decreased the ratio of HSL bound to ALDs (Fig. 3a, b). These results indicate that residues 489–659 are essential for LD binding.

We also measured the enzymatic activities of these HSL variants. When pNPB was used as the substrate, the activities of these variants were close to that of the full-length HSL (Fig. 3c). However, when the EnzChek lipase substrate was used, HSL(Δ 489–659) showed significantly decreased activity, while HSL(Δ 325–333) showed an activity similar to that of HSL(FL) (Fig. 3d).

Next, we checked the subcellular localization of HSL(FL) and HSL(Δ 489–659) in 3T3-L1 preadipocytes by fusing an enhanced green fluorescent protein (EGFP) to their C-termini and transiently expressing them in the 3T3-L1 preadipocytes. 3T3-L1 preadipocytes are a mouse cell line used to study fat cell formation and lipid accumulation⁴². The LDs in the cells were stained with LipidTOX Deep Red⁴³. The full-length HSL was expressed in the cytosol and showed an obvious accumulation around the LDs (Fig. 3e, top; Fig. 3f). In contrast, HSL(Δ 489–659) was widely distributed in the cytosol but not accumulated around the LDs (Fig. 3e, middle; Fig. 3f). Residues 489–659 alone with an EGFP fusing to its C-terminus accumulated on the LDs when transiently expressed in the 3T3-L1 preadipocytes (Fig. 3e, bottom; Fig. 3f). Similar results were also observed when we stably expressed these EGFP-fusion proteins in Huh-7 cells (Supplementary Fig. 3), a human liver cancer cell line frequently used to study lipid metabolism⁴⁴. These results are consistent with our findings in the flotation assay, which suggest that the regulatory domain (residues 489–659) is necessary and sufficient for the LD binding of HSL.

Identification of LD-binding regions in HSL using HDX-MS

To identify which regions in HSL are involved in binding with LDs, we also used hydrogen-deuterium exchange mass spectrometry (HDX-MS). HDX-MS measures the exchange rates of hydrogen atoms in protein amide groups with deuterium in the solvent.

Amide hydrogens involved in hydrogen bonds or buried away from the solvent exchange more slowly than those in flexible or solvent-accessible regions. Therefore, HDX-MS is widely used in the study of protein conformational changes and interactions involving proteins^{45,46}. The purified HSL was first mixed with the ALDs or the same volume of the assay buffer, then diluted with the same buffer prepared with D₂O to initiate the hydrogen-deuterium exchange. After 5, 30, or 600 s, the exchange was stopped by adding a quench buffer. The quenched sample was digested by pepsin online and subjected to UPLC/MS analysis (Fig. 4a; Supplementary Tables 2 & 3).

At each time point, we calculated the deuterium incorporation ratio for each digested peptide generated from both the ALD-bound and the ALD-free HSL samples (Fig. 4b; Supplementary Figs. 4 & 5). The region containing residues 480–640, which almost covers the whole regulatory domain, showed higher deuterium incorporation ratios than other regions in both samples. This finding is consistent with the cryo-EM data the predicted secondary structure of the regulatory domain, which mainly consists of a long flexible and unstructured loop (Fig. 4b). We then subtracted the deuterium incorporation ratios of the ALD-free HSL sample from these of the ALD-bound sample to quantify the changes in deuterium incorporation ratios upon ALD binding, and mapped these changes onto the structure of full-length HSL predicted by AlphaFold2 (ref. 47) (Fig. 4c). The AlphaFold2-predicted structure closely resembles the structure of each protomer in the cryo-EM structure of the HSL dimer (Fig. 2), but contains flexible regions that are invisible in the cryo-EM structure. Notably, the regulatory domain of HSL exhibited higher changes compared to other regions, with the most significant changes observed in an α -helix comprising residues 511–535 (Fig. 4c). These results are consistent with our finding that the regulatory domain is essential for LD binding, and suggest that the region containing residues 511–535 may be the core of the LD-binding region.

In addition, the HDX-MS data show that the deuterium incorporation ratios of certain peptides from the N-terminal 4-helix bundle decreased by more than 10% upon ALD binding. This suggests that the N-terminal 4-helix bundle may also be involved in the binding of HSL to lipid droplets.

Identification of the LD-binding motif in the HSL regulatory domain

To evaluate the findings from the HDX-MS data, and to identify the core region that is responsible for the LD-binding ability of the regulatory domain, we fused different truncations of the regulatory domain to the C-terminus of MBP (Fig. 5a), overexpressed them in *E. coli*, and purified them to homogeneity. We designed these constructs because residues 489–509 and residues 510–535 are predicted as two α -helices, while residues 536–659 are predicted as a flexible loop by AlphaFold2 (ref. 47).

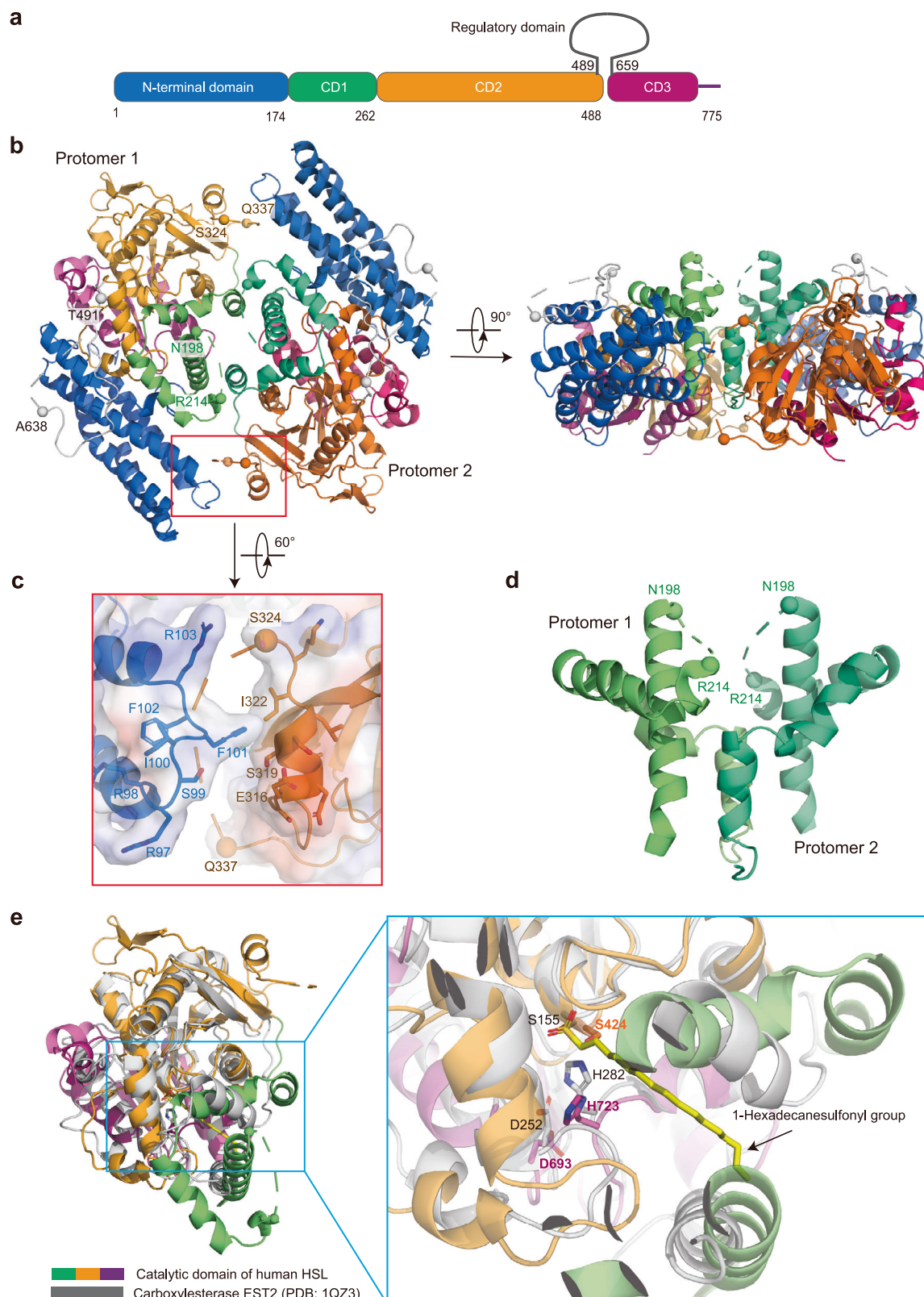


Fig. 2 | Cryo-EM structure of human HSL. a The color-coded diagram of human HSL. The catalytic domain (CD) of HSL consists of three subdomains: CD1, CD2, and CD3. **b** The overall structure of HSL. Residues between N198 and R214, between S324 and Q337, between T491 and A638 (the majority of the regulatory domain), and residues before R4 and after P752 were not built in the structure. **c** The dimer interface between the N-terminal domain of one protomer and the CD2 subdomain

of the other protomer. **d** The dimer interface between the CD1 subdomain from two HSL protomers. **e** Alignment of the cryo-EM structure of the catalytic domain of HSL with the crystal structure of the carboxylesterase EST2 (PDB: 1QZ3). The root mean square deviation (RMSD) over 1179 backbone atoms is 1.843 Å. EST2 is colored gray, with the 1-hexadecanesulfonyl group that mimics the substrate of EST2 colored yellow. The catalytic triads of HSL and EST2 are shown as sticks.

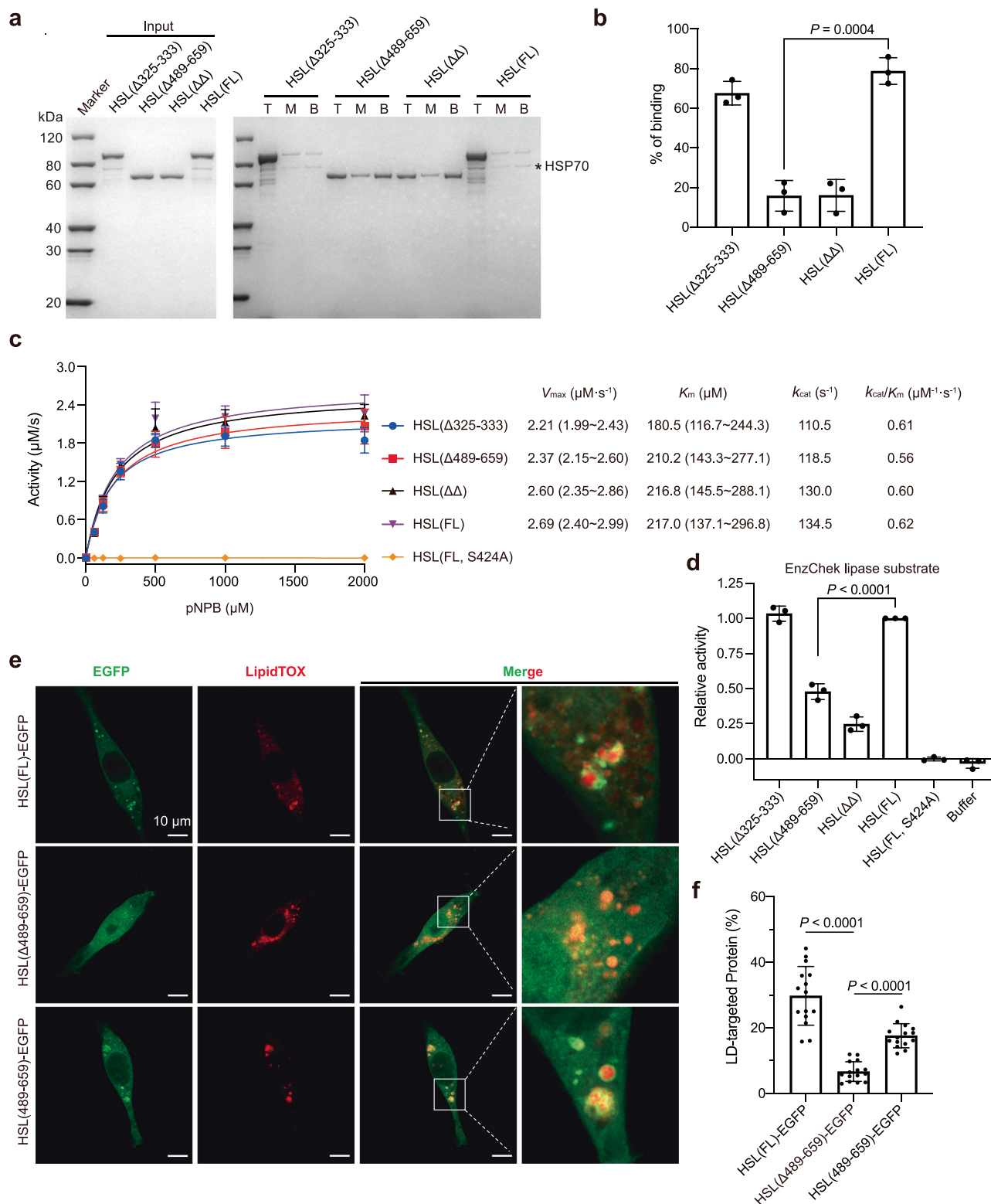


Fig. 3 | Identification of the regulatory domain as an LD-binding region in HSL.

a, b Evaluation of the ALD-binding abilities of full-length (FL) human HSL and its variants using the flotation assay. HSL(Δ325–333) and HSL(Δ489–659) are human HSL variants with residues 325–333 and 489–659 deleted, respectively. HSL(ΔΔ) refers to the human HSL variant with both residues 325–333 and residues 489–659 deleted. **c** Measurement of the enzymatic activities of FL HSL and its truncates using pNPB. Each k_{cat} value was calculated by dividing the corresponding V_{max} value by the concentration of HSL (20 nM) in the assay system. **d** Measurement of the enzymatic activities of FL HSL and its truncates using the EnzChek lipase substrate as the substrate. **e** Subcellular localization of human HSL and its variants in 3T3-L1 preadipocytes. HSL (FL), HSL (Δ489–659), and the regulatory domain (residues

489–659) of HSL, each with an EGFP fused to its C-terminus, were transiently expressed in 3T3-L1 preadipocytes. The cells were incubated with 0.2 mM oleic acid for 15 h, then fixed with 4% PFA and stained using LipidTOX Deep Red, a fluorescent dye to visualize neutral lipid accumulation. The images were taken by using a ZEISS LSM 980 microscopy. **f** Quantification of the EGFP signal of human HSL and its variants on lipid droplets in 3T3-L1 preadipocytes (a total of 15 cells were analyzed from three independent measurements.) The data in **a** and **e** each are the results of a representative experiment out of three independent experiments. The data in **b, c, d, and f** represent the mean \pm SD of three independent measurements. The data in **b, d, and f** were analyzed using the unpaired *t*-test in Prism to calculate the two-tailed *P*-values. Source data are provided as a Source Data_Fig. 3 file.

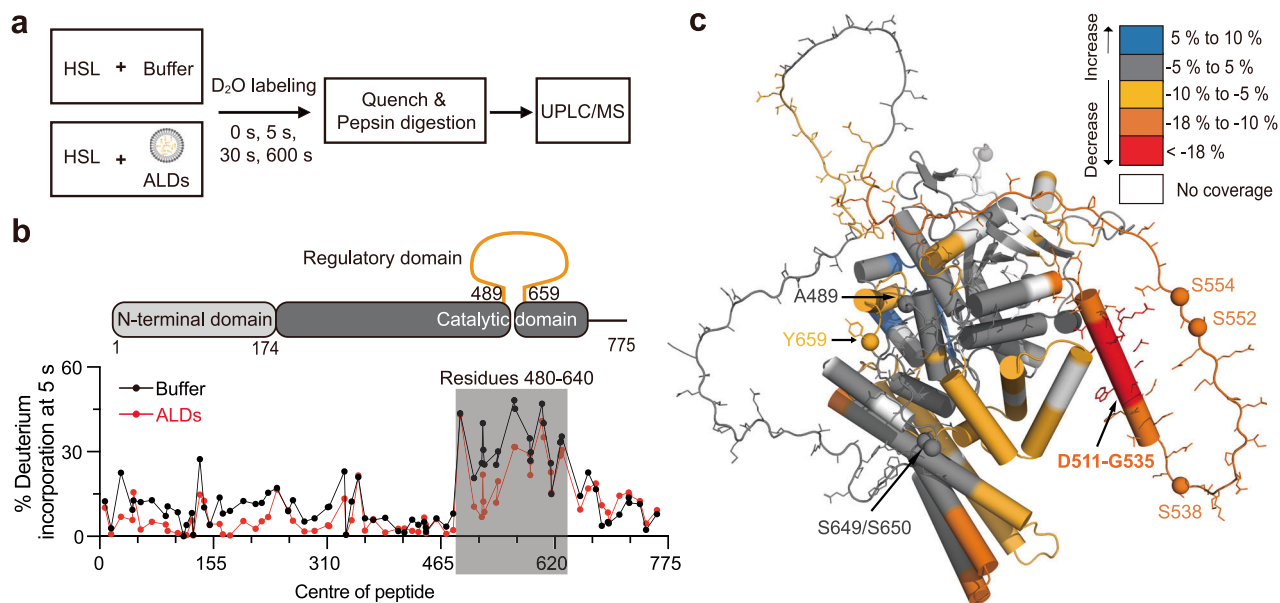


Fig. 4 | Identification of the LD-binding regions in HSL using HDX-MS. **a** The workflow of the HDX-MS experiment. The ALDs were prepared using a mixture of DOPC (75%) and DOPE (25%). Created in BioRender. Hu, Q. (2025) <https://BioRender.com/t74d619>. **b** Deuterium incorporation ratios of human HSL peptides after labeling the HSL by D₂O for 5 s in the absence or presence of ALDs. The x and y axes of each point represent the central residue of a single peptide and the deuterium incorporation ratio of that peptide. The gray box indicates residues that showed higher deuterium incorporation ratios than other regions in both groups.

c Changes in the deuterium incorporation ratios of human HSL upon association with ALDs were mapped on a structure of human HSL predicted by AlphaFold2 (ref. 47). Each peptide was colored based on the change in its deuterium incorporation ratio. The changes were calculated by subtracting the incorporation ratio of each peptide in the absence of ALDs from the incorporation ratio of the corresponding peptide in the presence of ALDs. Source data are provided as a Source Data Fig. 4 file.

We compared the LD-binding abilities of these fusion proteins with that of MBP alone using the flotation assay (Fig. 5b). We found that MBP fused with residues 489–659 of HSL, named MBP-HSL(489–659), had an ALD-binding ratio of about 30%. The ALD-binding ratio of MBP-HSL(489–538) was about 25%, slightly lower than that of MBP-HSL(489–659). In contrast, the ALD-binding ratio of MBP-HSL(539–659) was only about 8%, which is similar to that of MBP alone (Fig. 5b, c). MBP fused to a shorter construct, either residues 489–509 or residues 509–538, showed a significantly decreased ALD-binding ratio (Fig. 5b, c).

We then deleted residues 489–538 from HSL, referred to as HSL(Δ489–538), and tested its ability to bind to the ALDs using the flotation assay (Fig. 5d, e). The ALD-binding ratio decreased from 76% for HSL(FL) to 32% for HSL(Δ489–538). When transiently expressed in 3T3-L1 preadipocytes, HSL(Δ489–538) with an EGFP fused to its C-terminus lost the ability to bind to LDs (Fig. 5f, middle; Fig. 5g), in comparison with the HSL(FL)-EGFP fusion protein (Fig. 5f, top; Fig. 5g). In contrast, residues 489–538 fused with EGFP was accumulated around LDs in the 3T3-L1 preadipocytes (Fig. 5f, bottom; Fig. 5g).

Taken together, our data suggest that residues 489–538 of the regulatory domain are the LD-binding motif in the HSL regulatory domain. We named this motif the “H-motif”.

Aromatic residues in the H-motif are essential for LD binding

We further checked which residues in the H-motif are involved in LD binding. Previous studies reveal that membrane-binding motifs are typically rich in hydrophobic or amphipathic amino acids, allowing them to interact with the phospholipid layer². We first focused on residues 511–535 since our HDX-MS data suggest that this sequence may be the core of the LD-binding motif. According to the structure of the H-motif predicted by AlphaFold2 (ref. 47), three aromatic residues, including F519, W526, and F530, line up on the same side of the H-motif; while two positively charged residues, R517 and R520, are on the other side (Fig. 6a). We aligned the protein sequences of HSL from different species, and found that the H-motif is highly conserved in

species ranging from human to mice; residues 508–532 are also conserved in *Xenopus tropicalis* and *Danio rerio* (Fig. 6b).

We fused the wild-type human H-motif and its mutants to the C-terminus of MBP and overexpressed them in *E. coli*. The MBP fused with the WT H-motif, or with H-motifs carrying mutations F519V/W526V/F530V, F519A/W526A/F530A, and R517A/R520A, is named MBP-WT, MBP-3V, MBP-3A, and MBP-R2A, respectively. The LD-binding abilities of the purified proteins were evaluated using the flotation assay. We found that MBP-R2A had a similar ALD-binding ratio to that of MBP-WT, but MBP-3V and MBP-3A showed significantly decreased ALD-binding ratios (Fig. 6c, d), indicating that the three aromatic residues, but not the two arginine residues, are essential for LD binding. We also confirmed the importance of the three aromatic residues by testing the LD-binding ability of the H-motif when it's fused to EGFP and transiently expressed in 3T3-L1 preadipocytes. Mutating the three aromatic residues to alanine or valine almost completely disrupted the ability of the H-motif to bind to LDs (Fig. 6e, f).

The N-terminal 4-helix bundle is also an LD-binding motif in HSL

The HDX-MS data suggest that the N-terminal 4-helix bundle (residues 1–136) of HSL may also contribute to its LD-binding ability. We fused the 4-helix bundle to the C-terminus of MBP and found that this 4-helix bundle significantly increased the ALD-binding ratio of MBP (Fig. 7a, b).

Upon examining the AlphaFold2 predicted structure, we identified an amphipathic loop containing residues 97 to 103 (RRSIFFR) within this 4-helix bundle (Fig. 7c). We hypothesized that two hydrophobic residues, I100 and F101, in this loop are essential for the lipid droplet-binding ability of the 4-helix bundle. To test this, we introduced the I100A and F101A double mutations into HSL to generate the HSL mutant HSL(I100A/F101A), and introduced the H-motif mutations (F519A/W526A/F530A) into HSL to generate HSL(FL, 3A). By further combining the I100A and F101A mutations

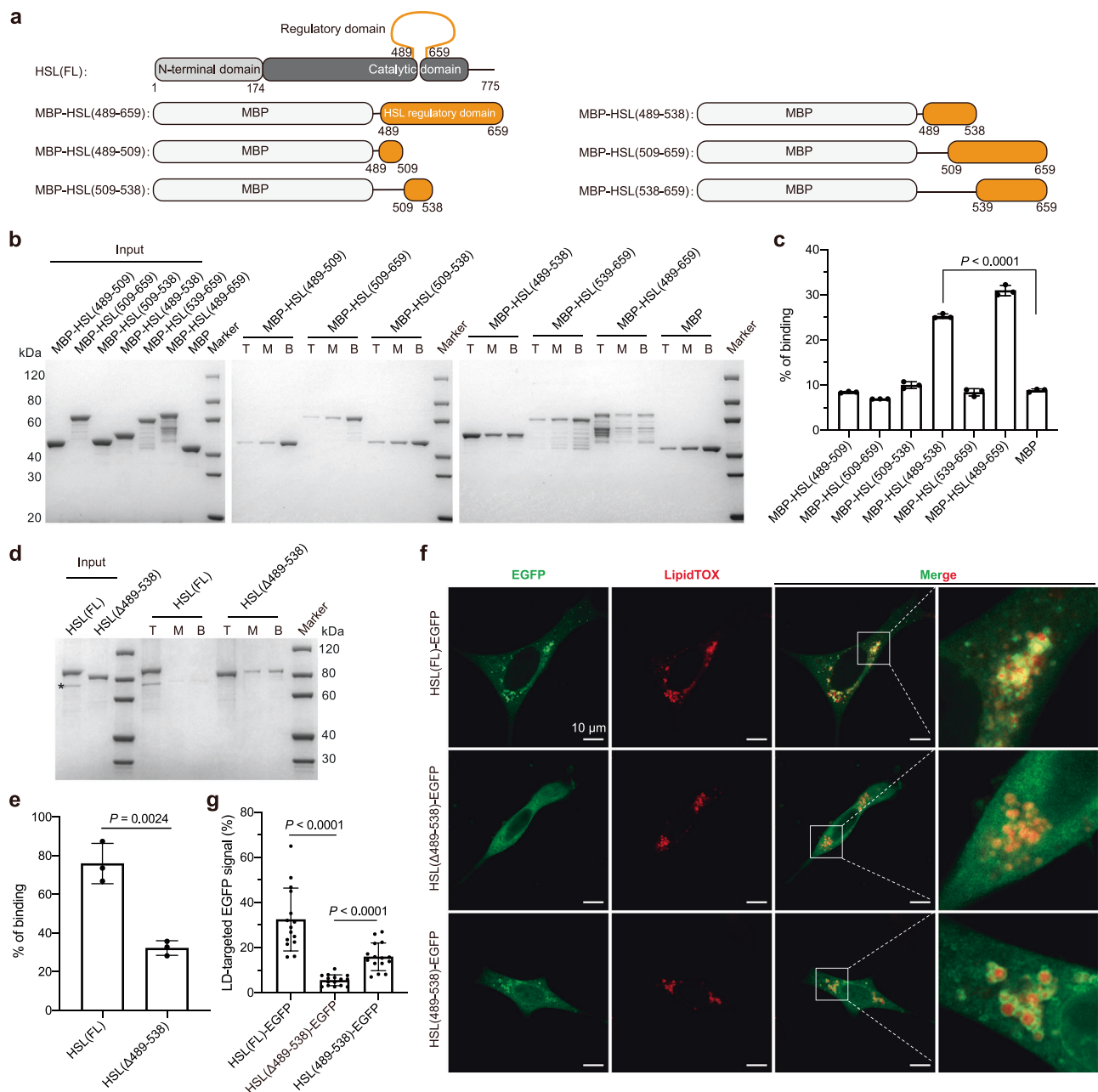


Fig. 5 | Residues 489–538 is the LD-binding motif in the HSL regulatory domain.

a The linear diagrams of full-length HSL and truncations of the HSL regulatory domain with an MBP fused to their N-termini. **b, c** Evaluation of the ALD-binding abilities of the MBP fusion proteins using the flotation assay. **d, e** Evaluation of the ALD-binding abilities of full-length HSL and HSL with residues 489–538 deleted using the flotation assay. **f** Subcellular localization of human HSL and its variants in 3T3-L1 preadipocytes. HSL (FL), HSL (Δ489–538), and the LD-binding motif (residues 489–538) of HSL, each with an EGFP fused to its C-terminus, were transiently

expressed in 3T3-L1 preadipocytes. Then the cells were treated and imaged as described in Fig. 3e. **g** Quantification of the EGFP signal of human HSL and its variants on lipid droplets in 3T3-L1 preadipocytes (a total of 15 cells were analyzed from three independent measurements). The data in **b, d, f** each are the results of a representative experiment out of three independent experiments. The data in **c, e, and g** represent the mean \pm SD of three independent measurements. The data in **c, e, and g** were analyzed using the unpaired *t*-test in Prism to calculate the two-tailed *P*-values. Source data are provided as a Source Data Fig. 5 file.

with the H-motif mutations, we generated another HSL mutant, HSL(FL, 5A). We found that the ALD-binding ratio of HSL(I100A/F101A) was significantly decreased compared to the wild-type HSL, and the ALD-binding ratio of HSL(FL, 5A) was even lower than that of HSL(I100A/F101A) (Fig. 7d, e). We also checked the LD-binding ability of these HSL mutants in 3T3-L1 preadipocytes, and the results are consistent with the ALD-binding results (Fig. 7f, g). These findings indicate that in addition to the H-motif, the N-terminal 4-helix bundle is also an LD-binding motif of HSL.

LD-binding motifs but not phosphorylation determine LD binding of HSL in 3T3-L1 preadipocytes

Phosphorylation is known to regulate the activity of HSL. Human HSL can be phosphorylated at S552, S649, and S650 by PKA^{10,11}, and phosphorylated at S554 by AMPK (corresponding to S565 in rat HSL⁴⁸). Upon treating 3T3-L1 adipocyte cells with isoproterenol (an agonist of β adrenoceptor) to promote cAMP production to activate PKA, rat HSL was reported to translocate from the cytosol to LDs, and mutating S659 and S660 of HSL to alanine blocked this translocation¹².

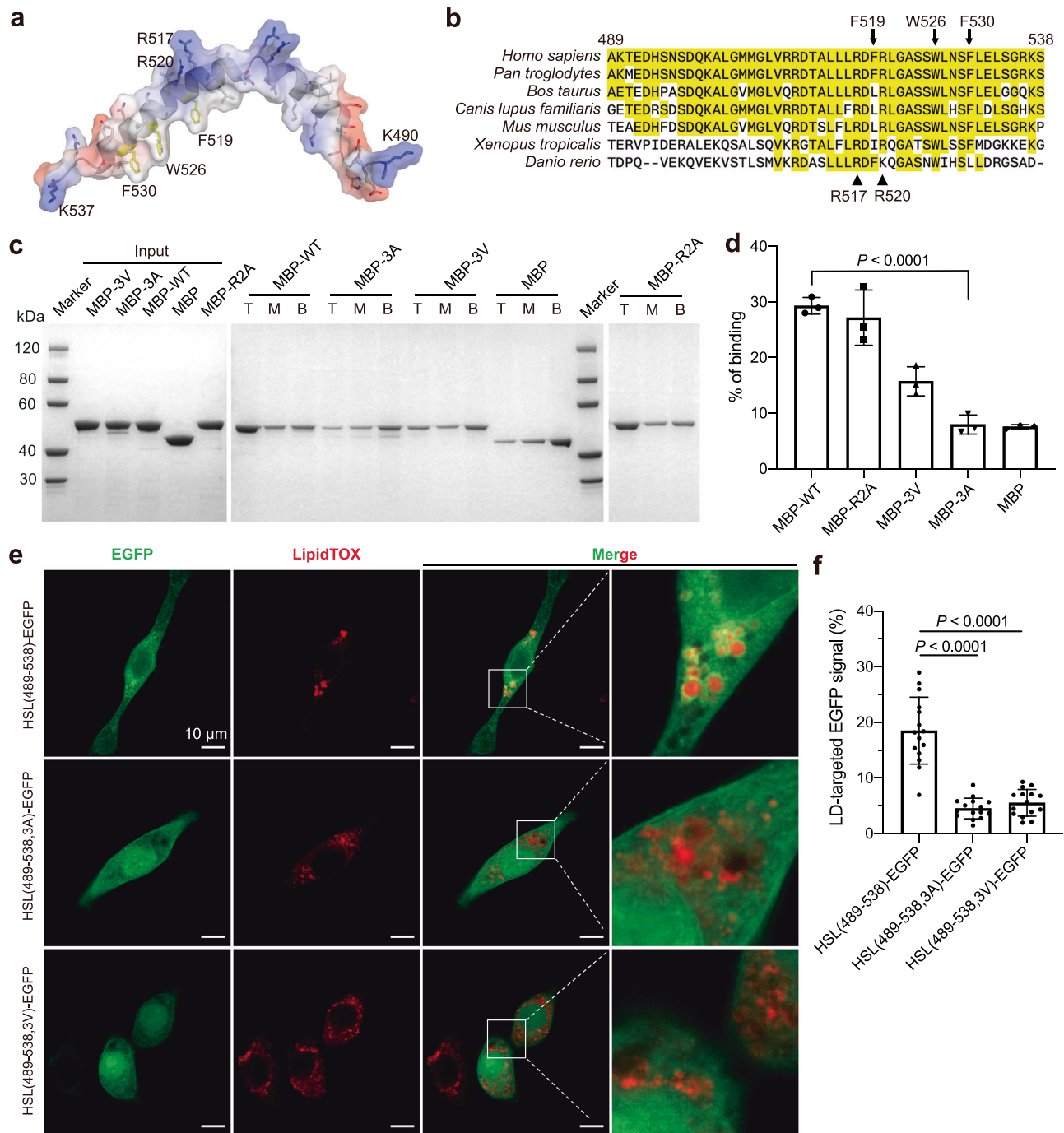
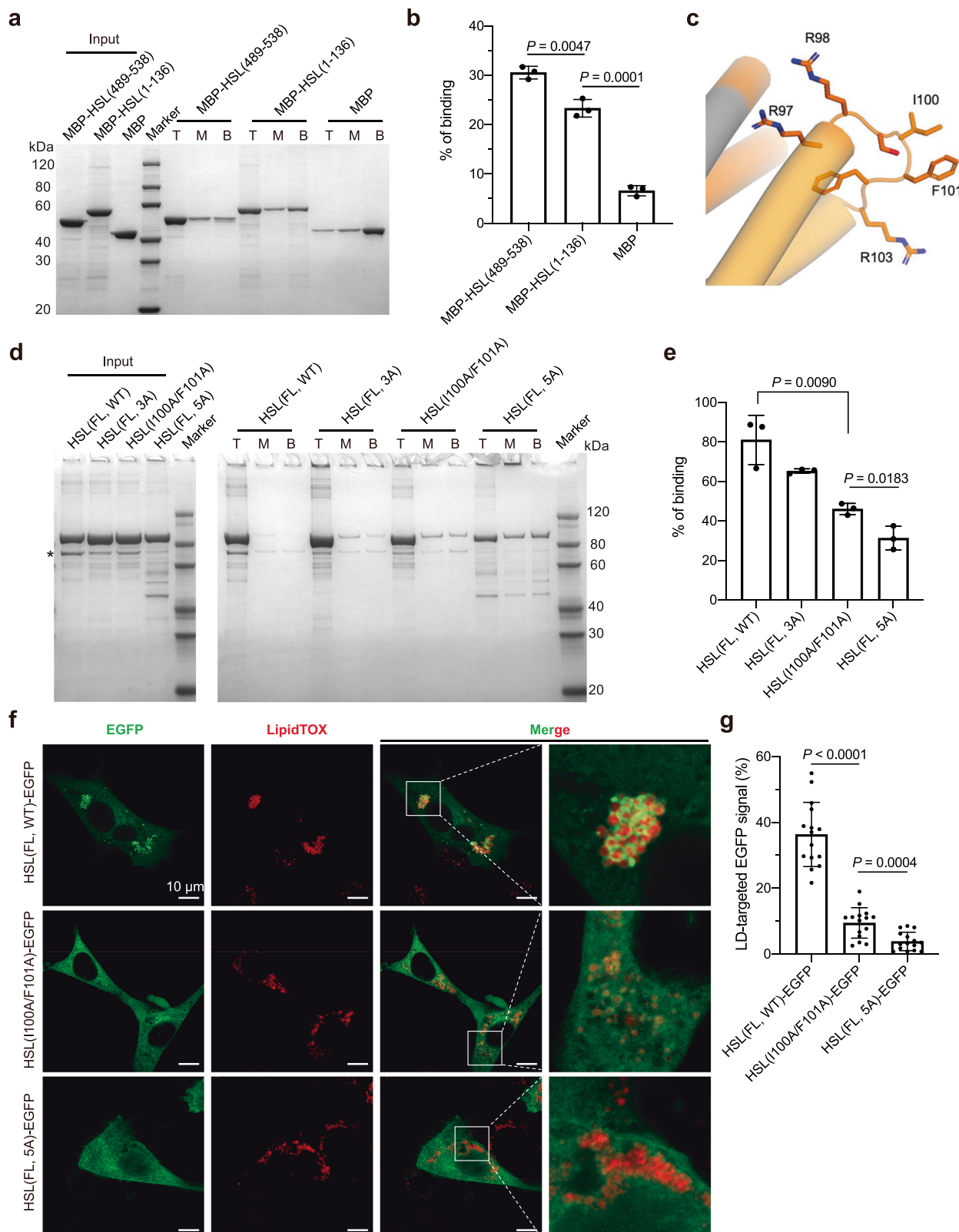


Fig. 6 | Identification of the key residues in the H-motif. **a** Structure of the H-motif predicted by AlphaFold2 (ref. 47). The protein contact potential was generated in PyMOL. **b** Alignment of the protein sequence of the H-motif in human HSL with these in HSL from other species using SnapGene. The three aromatic residues (F519, W526, F530) and the two arginine residues (R517, R520) were indicated by arrows and triangles, respectively. **c**, **d** Evaluation of the ALD-binding abilities of the human H-motif and its variants fused with an MBP at their N-termini using the flotation assay. MBP-WT represents the wild-type H-motif-MBP fusion protein, while MBP-3A, MBP-3V, and MBP-R2A represent MBP fusion proteins in which the H-motif carries the F519A/W526A/F530A triple mutations (3A), F519V/W526V/F530V triple mutations (3V), and R517A/R520A double mutations (R2A), respectively. **e** Subcellular localization of human H-motif and its variants in 3T3-L1

preadipocytes. The wild-type H-motif (residues 489-538), H-motif carrying the F519A/W526A/F530A triple mutations (3A), and that carrying the F519V/W526V/F530V triple mutations (3V), each with an EGFP fused to its C-terminus, were transiently expressed in 3T3-L1 preadipocytes. Then the cells were imaged as described in Fig. 3e. **f** Quantification of the EGFP signal of human H-motif and its variants on lipid droplets in 3T3-L1 preadipocytes (a total of 15 cells were analyzed from three independent measurements). The data in **c** and **e** are the results of a representative experiment out of three independent experiments. The data in **d** and **f** represent the mean \pm SD of three independent measurements. The data in **d** and **f** were analyzed using the unpaired *t*-test in Prism to calculate the two-tailed *P*-values. Source data are provided as a Source Data Fig. 6 file.



We first tested the effect of PKA activation on the subcellular localization of HSL in 3T3-L1 preadipocytes. We transiently expressed human HSL with an EGFP fused to its C-terminus in 3T3-L1 preadipocytes and then treated the cells with forskolin, an activator of adenylyl cyclases to promote cAMP production. Without forskolin treatment, HSL had already accumulated around the LDs, and forskolin treatment did not noticeably increase the accumulation (Fig. 8a, top;

Fig. 8b). The phosphorylation of HSL, induced by forskolin treatment, was verified by Western blot (Fig. 8c). Consistent with this finding, we found that the S552A/S649A/S650A triple mutant and the S552A/S544A/S649A/S650A quadruple mutant of human HSL maintained the ability to accumulate on the LDs in 3T3-L1 preadipocytes (Supplementary Fig. 6a). In addition, the S552E/S554E/S649E/S650E quadruple mutant, which mimics the phosphorylated state of HSL, showed an ALD-

Fig. 7 | Identification of the N-terminal 4-helix bundle as another LD-binding region in HSL. **a, b** Evaluation of the ALD-binding abilities of the H-motif and the N-terminal 4-helix bundle using the flotation assay. MBP-HSL(489-538) and MBP-HSL(1-136) refer to the H-motif and the N-terminal 4-helix bundle (residues 1-136) of HSL fused with an MBP to its N-terminus, respectively. **c** The AlphaFold2 predicted structure of the amphipathic loop containing residues 97 to 103 (RRSIFFR) in the N-terminal 4-helix bundle. **d, e** Evaluation of the ALD-binding abilities of HSL and its variants using the flotation assay. HSL(FL, 3A) is the full-length HSL carrying the F519A/W526A/F530A triple mutations. HSL(FL, 5A) carries two additional mutations, I100A and F101A, compare to HSL(FL, 3A). **f** Subcellular localization of

human HSL and its variants in 3T3-L1 preadipocytes. The wild-type HSL, HSL(I100A, F101A), and HSL(FL, 5A), each with an EGFP fused to its C-terminus, were transiently expressed in 3T3-L1 preadipocytes. Then the cells were imaged as described in Fig. 3e. **g** Quantification of the EGFP signal of human HSL and its variants on lipid droplets in 3T3-L1 preadipocytes (a total of 15 cells were analyzed from three independent measurements). The data in **a, d**, and **f**, each are the results of a representative experiment out of three independent experiments. The data in **b, e**, and **g** represent the mean \pm SD of three independent measurements. The data in **b, e**, and **g** were analyzed using the unpaired *t*-test in Prism to calculate the two-tailed *P*-values. Source data are provided as a Source Data_Fig. 7 file.

binding ability similar to that of the S552A/S554A/S649A/S650A quadruple mutant in the flotation assay (Supplementary Fig. 6b, c). We also evaluated the effect of phosphorylation on the LD-binding ability of HSL using purified dephosphorylated and phosphorylated HSL (Supplementary Fig. 7a, b), and found that phosphorylation had little effect on the ALD-binding ability of human HSL (Supplementary Fig. 7c–e).

We have identified that both the H-motif and the N-terminal 4-helix bundle are essential for the LD-binding ability of HSL. Deletion or mutation of either region can disrupt the colocalization of HSL with LDs (Figs. 5 & 7). To test whether LD-binding plays a role in the regulation of HSL by phosphorylation, we transiently expressed EGFP-fused wild-type HSL and its variants in 3T3-L1 preadipocytes and treated the cells with forskolin. Firstly, we confirmed that regardless of forskolin treatment, the HSL(FL, 3A) and HSL(FL, 5A) mutants could not accumulate on LDs (Fig. 8a, b). Similar results were observed when we fused mBaojin⁴⁹, a bright and stable monomeric GFP derived from StayGold, to the C-termini of wild-type HSL, HSL(Δ 489-538), and HSL(FL, 3A) (Supplementary Fig. 8). We also checked the effect of forskolin-induced phosphorylation on the subcellular localization of HSL in HEK 293T and Huh-7 cells, and the results are similar to these in 3T3-L1 preadipocytes (Supplementary Figs. 9 and 10). Secondly, we found that both HSL(FL, 3A) and HSL(FL, 5A) had similar phosphorylation levels as the wild-type HSL when transiently expressed in 3T3-L1 preadipocytes, and their phosphorylation levels were increased upon forskolin treatment (Fig. 8c). These results suggest that the LD-binding motifs are necessary for the binding of HSL to LDs but not for the phosphorylation of HSL in 3T3-L1 preadipocytes.

We also checked the effect of phosphorylation on the enzymatic activity of HSL using *in vitro* assays. We have shown that deletion of the regulatory domain decreased the activity of HSL to hydrolyze the EnzChek lipase substrate (Fig. 3d) but not the pNPB substrate (Fig. 3c). In consistent with this finding, deletion of the H-motif, or mutation of F519/W526/F530 to alanine or valine, affected the enzymatic activity of HSL in a similar way (Supplementary Fig. 7f, g). But phosphorylation showed minimal effect on the activity of HSL to hydrolyze the EnzChek lipase substrate (Supplementary Fig. 7h, i) or DAG (1,2 Dioleoyl-*rac*-glycerol), a natural substrate of HSL (Supplementary Fig. 7j, k). These findings indicate that phosphorylation has minimal effect on the enzymatic activity of purified HSL.

H-motif and phosphorylation independently influence the LD binding of HSL in 3T3-L1 adipocytes

The results from the 3T3-L1 preadipocytes assay are consistent with those from the ALD-binding assay. However, the LDs in 3T3-L1 preadipocytes lack certain components, such as PLIN1, compared to 3T3-L1 adipocytes⁵⁰. Therefore, we next examined the roles of the H-motif and phosphorylation in regulating the LD-binding ability of HSL in 3T3-L1 adipocytes (Fig. 9).

Firstly, we found that the colocalization of HSL(FL, WT) with LDs was enhanced upon forskolin treatment (Fig. 9a, top; Fig. 9b); such an enhancement was observed even when the H-motif was deleted (Fig. 9a, middle; Fig. 9b) but was absent when three phosphorylation sites (S552/S649/S650) in HSL were mutated to alanine (Fig. 9a,

bottom; Fig. 9b). Western blot analysis confirmed increased phosphorylation levels of both HSL(FL, WT) and the H-motif deleted mutant following forskolin treatment (Fig. 9c). These observations suggest that in 3T3-L1 adipocytes, PKA-catalyzed phosphorylation of HSL promotes its localization to LDs, independent of the H-motif.

Secondly, we found that deletion of the H-motif significantly reduced the colocalization of HSL with LDs, regardless of forskolin treatment (Fig. 9a, b). Moreover, the H-motif deletion did not affect forskolin-induced phosphorylation of HSL at S650 (Fig. 9c). These results indicate that the H-motif facilitates HSL localization to LDs in a phosphorylation-independent manner and does not influence PKA-catalyzed phosphorylation of HSL.

To understand the differences between the results from 3T3-L1 preadipocytes and those from 3T3-L1 adipocytes, we focused on PLIN1. We confirmed that the mRNA level of PLIN1 was very low in 3T3-L1 preadipocytes but significantly increased upon differentiation of 3T3-L1 preadipocytes into 3T3-L1 adipocytes (Supplementary Fig. 11a). Previous studies have reported that PLIN1 is a scaffold protein on LDs and can recruit HSL to LDs²¹, and this recruitment is regulated by PKA-catalyzed phosphorylation of PLIN1²². We examined the effect of PLIN1 on the LD-binding ability of HSL using the *in vitro* flotation assay. Unexpectedly, we found that PLIN1, in both its unphosphorylated and phosphorylated states, decreased the ALD-binding ability of purified HSL (Supplementary Fig. 11 b–i). These findings suggest that PLIN1, at least by itself, cannot explain the phosphorylation-dependent localization of HSL to LDs in 3T3-L1 adipocytes.

Discussion

We have identified the H-motif and the N-terminal 4-helix bundle of HSL as two LD-binding motifs of HSL, providing evidence that HSL can directly bind to LDs in the absence of the LD scaffold protein PLIN1 and elucidating the molecular mechanism for the LD binding of HSL. Though the possibility that HSL may be recruited to LDs through interactions with other LD-bound proteins cannot be excluded, our findings reveal that direct binding, mediated by the LD-binding motifs, is essential for the localization of HSL to LDs and may explain the LD binding of HSL in its basal state.

We have demonstrated that in 3T3-L1 preadipocytes, the binding of HSL to LDs is predominantly attributed to interactions mediated by the LD-binding motifs and is not affected by PKA-catalyzed phosphorylation (Fig. 8). In contrast, in 3T3-L1 adipocytes, PKA-catalyzed phosphorylation enhances HSL localization to LDs independently of the H-motif-mediated LD binding. The results in 3T3-L1 adipocytes are consistent with previous studies showing that phosphorylation of HSL by PKA induced the translocation of HSL from the cytosol to LDs^{12–14}. However, the H-motif remains essential for the localization of HSL to LDs in 3T3-L1 adipocytes, as its deletion significantly decreases the colocalization of HSL with LDs, regardless of PKA-catalyzed phosphorylation (Fig. 9). Taken together, these findings suggest that in 3T3-L1 adipocytes, HSL localizes to LDs through two distinct mechanisms: one dependent on PKA-catalyzed phosphorylation and the other mediated by the LD-binding motifs, which operates independently of PKA-catalyzed phosphorylation.

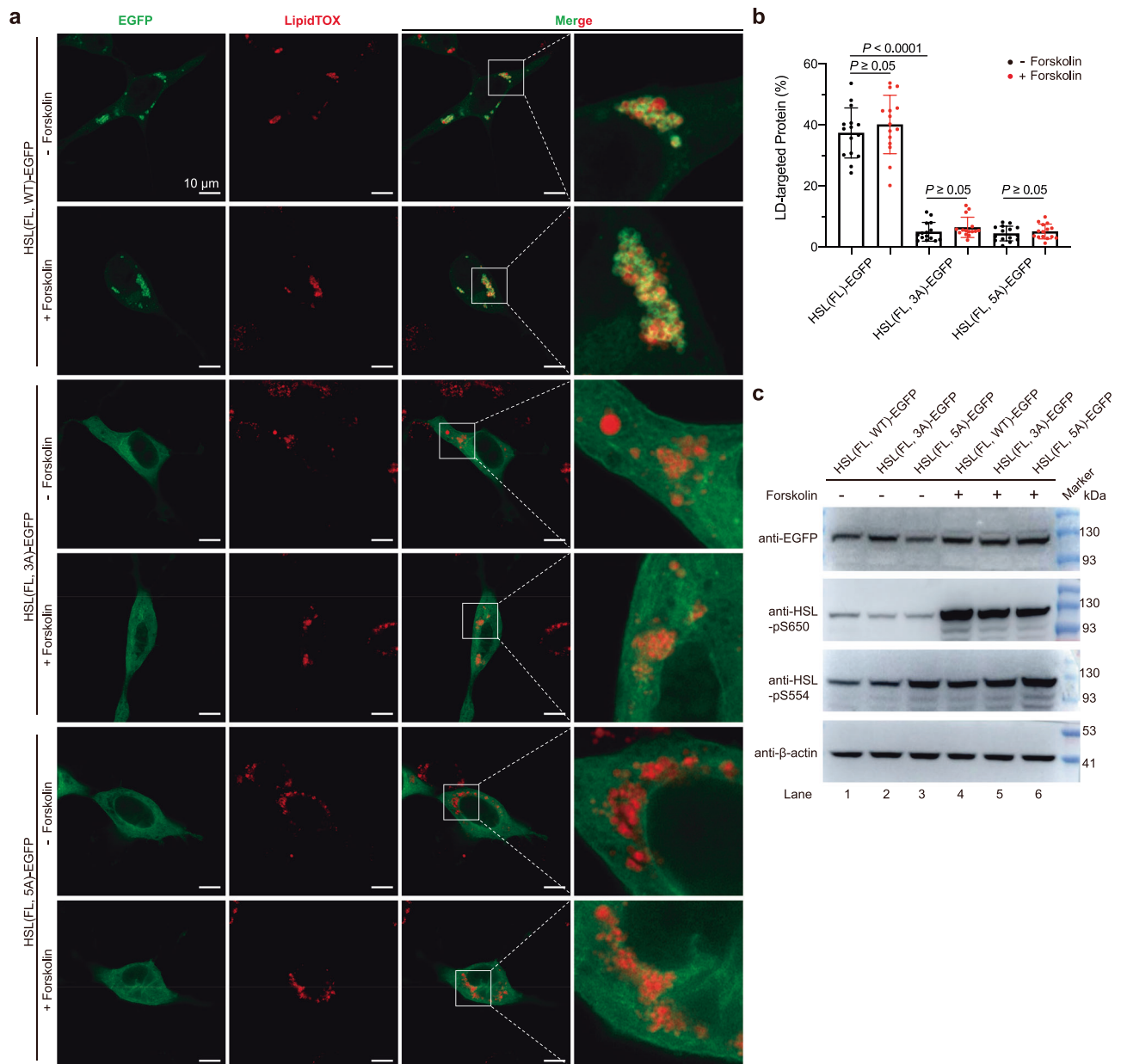


Fig. 8 | LD-binding and phosphorylation of HSL are independent processes in 3T3-L1 preadipocytes. **a** Subcellular localization of human HSL and its variants in 3T3-L1 preadipocytes. The cells were treated with 1 mM IBMX (a PDE inhibitor) and 10 μ M forskolin or the same volume of DMSO control. Wild-type HSL, HSL(FL, 3A), and HSL(FL, 5A), each with an EGFP fused to its C-terminus, were transiently expressed in 3T3-L1 preadipocytes. The cells were imaged as described in Fig. 3e. **b** Quantification of the EGFP signal of human HSL and its variants on lipid droplets in 3T3-L1 preadipocytes (a total of 15 cells were analyzed from three independent

measurements). **c** Upon treatment with forskolin or DMSO, the protein expression and phosphorylation levels of human HSL and its variants in 3T3-L1 preadipocytes were analyzed using Western blot. The data in **a** and **c**, are the results of a representative experiment out of three independent experiments. The data in **b** represent the mean \pm SD of three independent measurements. The data in **b** were analyzed using the unpaired *t*-test in Prism to calculate the two-tailed *P*-values. Source data are provided as a Source Data Fig. 8 file.

We have demonstrated that phosphorylation had minimal effects on the enzymatic activity of purified HSL and on the LD-binding ability of both purified HSL and HSL expressed in 3T3-L1 preadipocytes (Supplementary Figs. 6–10). These findings suggest that the observed enhancement of HSL localization to LDs in 3T3-L1 adipocytes, induced by forskolin treatment, may not be a direct effect of PKA-catalyzed HSL phosphorylation. Other factors present in 3T3-L1 adipocytes but not in 3T3-L1 preadipocytes may be involved in this enhancement. PLIN1 appears to be such a factor, given that previous studies have reported that phosphorylated PLIN1 can recruit HSL to LDs^{22,51}. However, our *in vitro* data showed that both unphosphorylated and phosphorylated PLIN1 negatively affect the LD-binding ability of purified HSL

(Supplementary Fig. 11 b-i). Thus, we propose that additional factors beyond PLIN1 are likely involved and remain to be identified.

Two types of motifs have been identified to directly associate with LDs in previous studies⁵². One is amphipathic α helices, which undergo conformational changes from a disordered structure to an amphipathic α helix upon association with the membrane^{46,52}. These amphipathic α -helices align parallel to the membrane surface when they associate with it^{46,52}. The other is hydrophobic regions, usually hydrophobic hairpins, that insert into the membrane^{52,53}. The H-motif identified in our study is predicted by AlphaFold2 to form two short helices connected by two arginine residues (Fig. 6). A recent study reported that a hairpin structure adopts a shallow open-V shape

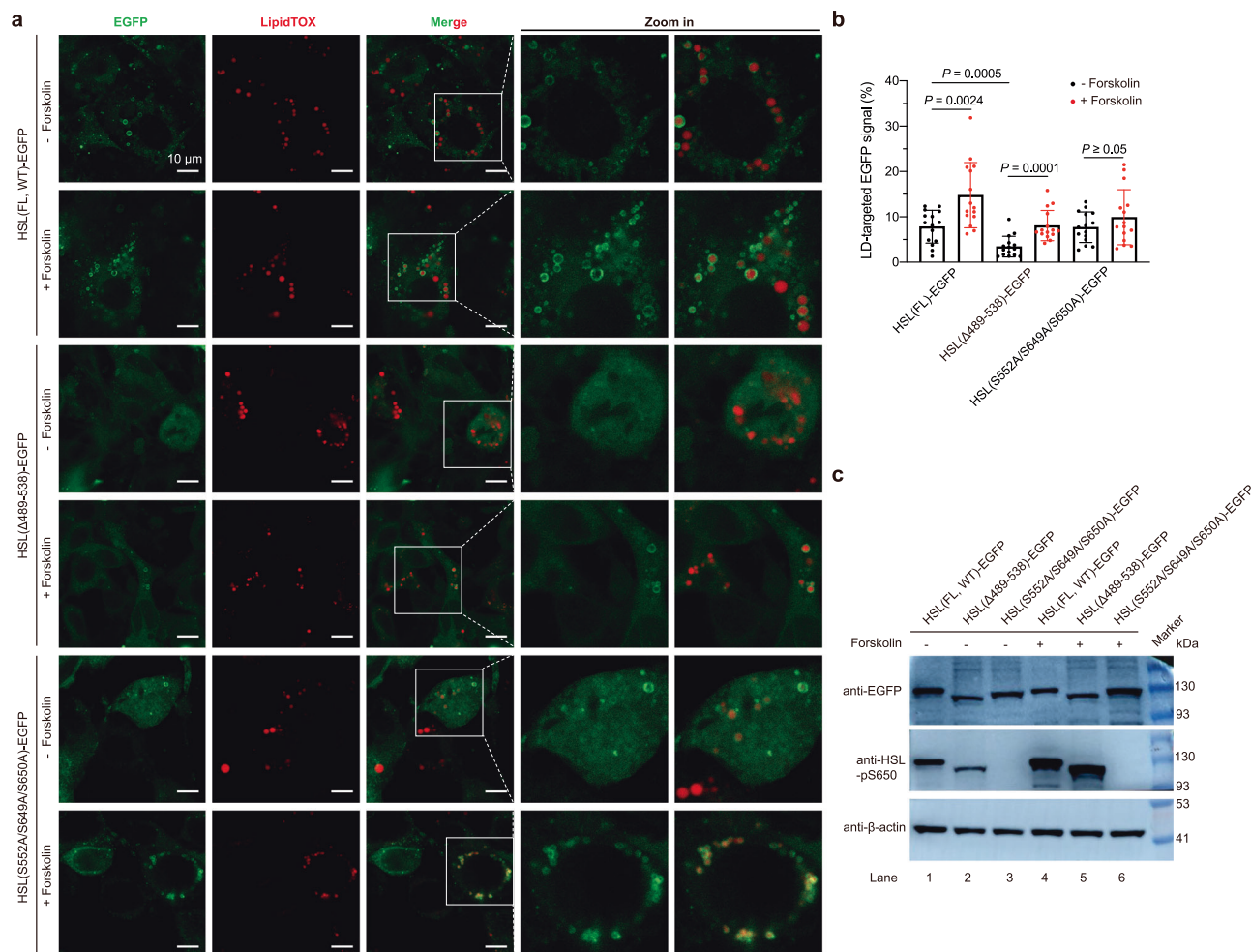


Fig. 9 | Evaluation of the role of the H-motif and phosphorylation in the LD binding of HSL in 3T3-L1 adipocytes. **a** Subcellular localization of human HSL and its variants in 3T3-L1 adipocytes. Wild-type HSL, HSL with the H-motif (residues 489–538) deleted, and full-length HSL carrying the phosphorylation site mutations (S552A/S649A/S650A), each with an EGFP fused to its C-terminus, were stably expressed in 3T3-L1 preadipocytes. The 3T3-L1 preadipocytes were then induced to differentiate into mature 3T3-L1 adipocytes using dexamethasone, IBMX, and insulin (see Methods). The 3T3-L1 adipocytes were treated with 1 mM IBMX and 10 μ M forskolin or the same volume of DMSO control, then the adipocytes were

imaged as described in Fig. 3e. **b** Quantification of the EGFP signal of human HSL and its variants on lipid droplets in 3T3-L1 adipocytes (a total of 15 cells were analyzed from three independent measurements). **c** Upon treatment with forskolin or DMSO, the protein expression and phosphorylation levels of human HSL and its variants in 3T3-L1 adipocytes were analyzed using Western blot. The data in **a** and **c**, are the results of a representative experiment out of three independent experiments. The data in **b** represent the mean \pm SD of three independent measurements. The data in **b** were analyzed using the unpaired *t*-test in Prism to calculate the two-tailed *P*-values. Source data are provided as a Source Data Fig. 9 file.

conformation when it associates with the phospholipid monolayer of LDs⁵³. We speculate that the H-motif may be associated with LDs through a mechanism similar to that of hydrophobic hairpins. Regarding the N-terminal 4-helix bundle of HSL, the other LD-binding motif identified in our study, it may be classified into hydrophobic regions and may interact with LDs through one end of the 4-helix bundle structure, which contains an amphipathic loop (residues 97 to 103: RRSIFFR) (Figs. 4 & 7). Further studies to figure out the coordination between the H-motif and the N-terminal 4-helix bundle when they bind to LDs, as well as the effects of the LD-binding on the overall structure of HSL, are important for understanding the functional mechanism of HSL.

Previous studies suggest that HSL can form homodimers^{54,55}. Shen et al. reported that the HSL from rat adipose tissue formed homodimers, and the enzymatic activity of dimeric HSL was about 40-fold higher than that of monomeric HSL⁵⁴. Krintel et al. reported that all three isoforms of HSL recombinantly expressed in insect cells mainly formed head-to-head homodimers in the negative stain electron microscopy (EM) images⁵⁵. In our study, we have determined the cryo-EM structure of human HSL, in which HSL forms a homodimer, but the

dimers are assembled by two HSL protomers through head-to-tail interactions (Fig. 2b–d). The CD1 subdomain of HSL, which is less conserved in bacterial homologs of human HSL, is located at the center of the HSL homodimer (Fig. 2b, d). Structural alignment suggests that the CD1 subdomain may interact with the acyl chains of its natural substrates, DAGs (Fig. 2e). However, the formation of the homodimer seems to block access to the catalytic residue S424 of HSL (Fig. 2e). In addition, the key residues in the 4-helix bundle, which mediate the LD-binding of HSL, are buried by the dimer interface, indicating that the dimer may dissociate upon binding to LDs. One possibility is that the observed homodimer in the cryo-EM structure represents an inactive state of HSL, and binding of HSL to LDs may dissociate the homodimer, thereby activating HSL. Further studies are required to test this hypothesis.

Methods

Genes and cloning

The cDNA of the human testis HSL (LIPE, 1076 aa, accession number in PubMed: NP_005348.2) and human PLIN1 (NM_002666) were purchased from YouBio. The HSL in our study refers to the adipocyte

isoform of human HSL (UniProt: Q05469-2), which contains only residues 302–1076 of the testis isoform. For protein expression and purification, the gene encoding adipocyte HSL and the gene encoding PLIN1 with a C-terminal FLAG tag were cloned into a pCAGGS vector. The regulatory domain (residues 489–659) of human HSL and its variants were each cloned into a modified pET15d vector. The expressed constructs each have an N-terminal maltose-binding protein (MBP) tag followed by a DrICE cleavage site. For cell assays, the gene encoding adipocyte HSL with an N-terminal FLAG tag and a C-terminal EGFP was cloned into a pcDNA3.1 vector. Site-directed mutagenesis was performed to generate the expression constructs of HSL variants.

Expression and purification of human HSL, HSL variants, and PLIN1

The plasmid of Human HSL in the pCAGGS vector was transfected in Expi293F cells (Invitrogen). Cells were cultured in SMM 293-TI Expression Medium (Sino Biological) at 37 °C with 5% CO₂ to a density of 2×10^6 cells per mL. For 0.8 L cell culture, 1.5 mg of HSL(FL) plasmid was pre-mixed and transfected with 3 mg of polyethylenimines (PEIs, Polysciences). The transfected cells were cultured for 58 h, then harvested by centrifugation at $3000 \times g$ for 10 min and resuspended in a lysis buffer (25 mM Tris-HCl pH 8.0, 150 mM NaCl, 5% Glycerol, 5 mM ATP, 5 mM MgCl₂) supplemented with a protease inhibitor cocktail (1.3 µg/mL aprotinin, 5 µg/mL leupeptin, 1 µg/mL pepstatin). The cells were lysed by incubating with 1.0% n-Dodecyl-β-D-Maltopyranoside (DDM) at 4 °C for 1 h. The cell lysate was centrifuged at $20,000 \times g$ for 1 h at 4 °C, then the supernatant was collected and incubated with anti-FLAG tag affinity resin (GenScript, Inc. Cat. No.: L00432-25) at 4 °C for 2 h. After washing the beads with buffer A (25 mM Tris-HCl pH 8.0, 150 mM NaCl, 5% Glycerol, 0.02% DDM), and buffer B (25 mM Tris-HCl pH 8.0, 150 mM NaCl, 5% Glycerol, 0.02% DDM, 5 mM ATP, 5 mM MgCl₂), the target protein was eluted using buffer A plus 0.4 mg/mL FLAG peptide (EveryLab, Cat No: PF01-50). The eluate was concentrated and further purified by gel filtration (Superdex 200 increase, 10/30, GE Healthcare) with a running buffer containing 25 mM Tris-HCl pH 8.0, 150 mM NaCl, and 0.01% GDN. The peak fractions were collected and used for cryo-EM sample preparation and biochemical assays. The PLIN1 and the HSL variants each have a C-terminal FLAG tag and were expressed and purified following the same protocol, except that the eluate of PLIN1 was concentrated and purified by gel filtration (Superdex 200 increase, 10/30, GE Healthcare) with a running buffer containing 25 mM Tris-HCl pH 8.0, 150 mM NaCl, 0.02% DDM, and 0.002% cholesteryl hemisuccinate Tris salt (CHS, Anatrace).

Expression and purification of MBP and MBP fusion proteins

The plasmids of MBP and MBP fusion proteins in the modified pET15d vector were transformed into BL21(DE3) cells. The transformed cells were grown in LB medium supplemented with 100 µg/mL ampicillin at 37 °C until OD₆₀₀ reached 0.8–1.0, and then cooled to 18 °C followed by the addition of 0.5 mM β-D-thiogalactopyranoside (IPTG). The cells were cultured at 18 °C for additional 15 h, and then harvested by centrifugation at $4000 \times g$ for 10 min and resuspended in a lysis buffer (25 mM Tris-HCl pH 8.0, 150 mM NaCl, 5% Glycerol, 1 mM DTT). After adding the protease inhibitor PMSF (1 mM), the cells were immediately disrupted by ultrasonication. The cell lysate was incubated with 1% DDM for 1 h, and then centrifuged at $20,000 \times g$ for 1 h at 4 °C. The supernatant was incubated with MBP Resin (Dextrin Beads, Smart-Lifescience, Cat. No.: SA077025) at 4 °C for 2 h, then the resin was washed with a wash buffer (25 mM Tris-HCl pH 8.0, 150 mM NaCl, 5% Glycerol, 1 mM EDTA, 1 mM DTT, 0.02% DDM). The protein was eluted from the resin with an elution buffer B (25 mM Tris-HCl pH 8.0, 150 mM NaCl, 5% Glycerol, 1 mM EDTA, 1 mM DTT, 0.02% DDM, 10 mM maltose). The eluate was concentrated and further purified by gel filtration (Superdex 200 increase, 10/30, GE Healthcare) with a running buffer

containing 25 mM Tris-HCl pH 8.0, 150 mM NaCl, and 0.01% GDN. The peak fractions were pooled and concentrated and then used for flotation assay.

Hydrogen deuterium exchange mass spectrometry

80 µL of purified HSL (17.8 µM in 25 mM Tris-HCl pH 8.0, 150 mM NaCl) was incubated for 1 h at room temperature with 40 µL of ALDs (OD₆₀₀ = 21.98) in an assay buffer (25 mM HEPES pH 7.4, 150 mM NaCl) or with 40 µL of the assay buffer without ALDs. The HDX reactions were initiated by adding 34 µL of labeling buffer (25 mM HEPES, 150 mM NaCl in D₂O, pD = 7.4) to 6 µL of the HSL sample, giving a final concentration of 85% D₂O. The exchange reaction was carried out for 0, 5, 30, and 600 s (each time point was carried out in triplicate). The reaction was quenched by adding 40 µL of quench buffer (0.7 M guanidine-HCl, 1.05% Formic acid) on ice. Then 65 µL of each sample was rapidly injected into a M-class UPLC system with HDX manager (Waters) and run over an Enzymate BEH Pepsin column (Waters, 2.1 × 30 mm, 5 µm) at 15 °C with a flowrate of 100 µL/min for 4 min. The digested peptic peptides were trapped into a VanGuard precolumn (Waters, 2.1 × 5 mm, 1.7 µm) and subsequently separated by an inline Acquity BEH C18 UPLC column (Waters, 1.0 × 100 mm, 1.7 µm). The mobile phases were 0.1% formic acid in water (A) and 0.1% formic acid in acetonitrile (B). The gradient of mobile phase B was increased from 2% to 35% in 6 min, with a flow rate of 50 µL/min. It was then held at 35% for 1 min and further increased to 85% in 0.5 min. After being held at 85% for 1 min, the gradient was decreased to 2% in 0.5 min and maintained for the post-equilibration. Mass spectra were acquired on a Synapt XS mass spectrometer (Waters) using an electrospray ionization source operated at 80 °C and a spray voltage of 3.0 kV. The mass range was from 50 to 2000 m/z. The MS^E method was used for peptide fragmentation and mapping (Low trap collision energy of 4 V and High ramp trap collision energy of 20–45 V).

According to the guidelines³⁶, the summary of the HDX-MS experiment details was presented in Supplementary Table 2. The peptide mapping was performed using ProteinLynX Global Server 3.03 software from Waters, with the processing parameters detailed in Supplementary Table 3. Then, the peptides were filtered upon importing into DynamX with these parameters: the Minimum intensity is 1481; the Minimum and Maximum sequence lengths are 3 and 0, respectively; the Minimum products is 2; the Minimum products per amino acid is 0.11; the consecutive products is 1; the Minimum sum intensity for products is 472; the Minimum score is 6.62; the Maximum MH⁺ error (ppm) is 10; the Replication-File threshold is 3. Next, the deuterium incorporation of each peptic peptide was automatically annotated using the DynamX. All peptides were manually inspected for correct charge state, correct retention time, and appropriate selection of isotopic distribution. The fully denatured HSL protein served as the maximally labeled control, with an average back-exchange degree of 29.87%. The deuterium incorporation ratios of the ALD-free HSL sample were subtracted from those of the ALD-bound sample to calculate the changes in deuterium incorporation ratios upon LD binding. These changes were mapped onto the structure of full-length HSL predicted by AlphaFold2. Following a protocol described⁴⁶, differences in exchange in a peptide were considered significant if they met all three of the following criteria: > 5% change in exchange, > 0.4 Da mass difference in exchange, and a *P*-value ≤ 0.01 using a two-tailed Student's *t*-test.

Measurement of the HSL activity using the EnzChek lipase substrate

The assay was done by following the protocol in a previous study with slight changes⁵⁷. Specifically, the EnzChek lipase substrate (Invitrogen, REF E33955) was prepared as a 100 µM stock in DMSO. The stock was

diluted to 0.75 μM using a reaction buffer containing 25 mM HEPES pH 7.4, 150 mM NaCl, and 1.5% fatty acid-free BSA (GOLDBIO, CAS: 9048-46-8). 20 μL of the diluted EnzChek lipase substrate was mixed with 5 μL of HSL (100 nM) in 25 mM Tris-HCl pH 8.0, 150 mM NaCl, and 0.01% GDN in a black 384-well plate (Corning, REF 3575) at 37 °C. The fluorescence signals were immediately monitored in a microplate reader (Spark) with an excitation wavelength of 482 nm and an emission wavelength of 515 nm. The fluorescence signals increased linearly, at least within 300 s. The signals were then converted to the concentration of BODIPY-C12 (Invitrogen, Cat. No.: D3823), which is a product of the EnzChek lipase substrate hydrolysis reaction, and then the slope of the curve from 0 to 200 s was calculated to measure the catalytic activity of HSL.

Measurement of the HSL activity using pNPB

The pNPB assay was done by following the protocol in a previous study³⁰. Specifically, the *p*-nitrophenyl butyrate (Bide Pharmatech Co., Ltd., CAS: 2635-84-9) was prepared as a 200 mM stock in acetonitrile and diluted to 1.25 mM using a reaction buffer containing 25 mM HEPES pH 7.4 and 150 mM NaCl. 20 μL of the diluted pNPB was mixed with 5 μL of HSL (100 nM) in 25 mM Tris-HCl pH 8.0, 150 mM NaCl, and 0.01% GDN in a transparent 384-well plate (Corning, REF 3640) at 37 °C. The absorbance at 380 nm was immediately monitored in a microplate reader (Spark). The K_m and k_{cat} were calculated using the Michaelis-Menten equation with GraphPad Software (GraphPad Inc., USA).

Measurement of the HSL activity using native substrate DAG

Native substrate DAG (1,2 Dioleoyl-*rac*-glycerol) (Sigma, Cat. No.: D8394) was used to measure the enzymatic activities of HSL and HSL($\Delta 489$ -538) in their unphosphorylated and phosphorylated states. DAG was prepared as a 1 mM stock in DMSO and diluted to 100 μM using a reaction buffer containing 25 mM HEPES pH 7.4, 150 mM NaCl, 1.5% BSA. 15 μL of the diluted DAG substrate was incubated with 15 μL of different phosphorylation states' HSL or HSL($\Delta 489$ -538) (74 nM) at room temperature. The enzymatic reactions were stopped by adding 5 μL of isopropyl alcohol containing 10% formic acid. Subsequently, 60 μL of methanol, 210 μL of MTBE, and 60 μL of ultrapure water were added, and the mixture was vortexed for 30 s and then centrifuged for 10 min at 20,000 $\times g$. Then, 150 μL of the supernatant was transferred to a fresh 1.5 mL microtube, and the organic solvent in the tube was slowly evaporated under nitrogen. The samples were then redissolved in the buffer containing 65% isopropyl alcohol, 30% acetonitrile, and 5% water. 50 μL of redissolved samples were added to a 384-well plate, and the plate was transferred to the Acoustic Ejection Mass Spectrometry (SCIEX, EchoTM MS) device for MS analysis. The amount of the released free fatty acid in each reaction was calculated according to the standard curve using oleic acid (aladdin, CAS: 112-80-1).

Cryo-EM sample preparation and data acquisition

4 μL of the purified HSL protein (1.14 mg/mL in 25 mM Tris-HCl pH 8.0, 150 mM NaCl, and 0.01% GDN) was incubated with HSL-IN-1 (100 μM) at 4 °C for 2 h. The sample was then applied onto a freshly glow-discharged holey carbon grid (Quantifoil, Au 300 mesh, RL2/1.3), blotted for 4 s, and rapidly plunged into liquid ethane using Vitrobot Mark IV operating at 8 °C and 100% humidity. Movies were recorded on a Titan Krios at 300 kV equipped with a Gatan K3 Summit direct electron detector and GIF Quantum energy filter (slit width 20 eV, Gatan) in super-resolution mode.

Structure determination and model building

All structure determination procedures were performed in cryoSPARC⁵⁸. A workflow chart is available in Supplementary Fig. 1. In summary, 15,292 micrographs went through patch-based CTF estimation and iterative particle auto-picking, yielding 21,915,892

particles, which were subjected to multiple rounds of 2D classifications, resulting in 429,837 selected particles. Among them, the “laid-down” views (the first three classes in the representative 2D images of the workflow chart) were found to dominate. Therefore, to generate a reliable initial model, these particles underwent 2D class rebalancing, resulting in 157,244 particles with evenly distributed views. Subsequently, these particles were subjected to a round of ab-initio reconstruction (number of classes = 2, maximum resolution = 5 Å) with C1 symmetry applied, where 25,625 particles (16.3%) produced an initial map with a monomeric shape and 131,619 particles (83.7%) produced an initial map with a dimeric shape. Next, these particles were applied for non-uniform refinement, generating a monomeric shape map at a resolution of 6.8 Å and a dimeric shape map at a resolution of 3.7 Å with C2 symmetry applied. To further enhance the resolution to a level where side chain densities are more discernible, seed-facilitated 3D classifications⁵⁹ were applied to the initial auto-picked 21,915,892 particles, using the 3.7 Å map as the good reference and four bad references generated by refining noise to high frequencies with a reversed protein mask. The seed-facilitated 3D classifications were performed sequentially under four-fold, two-fold, and one-fold binnings, progressively sieving particles from 5,509,131 to 3,110,919, and finally to 384,309. Ultimately, the 384,309 particles were used for non-uniform refinement, resulting in a map with a final resolution of 3.4 Å with C2 symmetry applied.

The HSL homodimer was manually built using Coot⁶⁰. Two copies of the AlphaFold2 prediction⁴⁷ of the human HSL monomer were manually fitted into the density map to serve as the starting model. The model was then manually adjusted, using aromatic residues as landmarks due to their clear visibility in the cryo-EM map. Each residue was carefully inspected, with their chemical properties considered during modeling. In total, 1150 amino acid residues were modeled. The model was subsequently refined in Phenix⁶¹, employing with secondary structure and geometry restraints to prevent overfitting. Statistics related to data collection, 3D reconstruction, and model refinement can be found in Supplementary Table 1. All figures in this article related to HSL structure were generated using PyMOL⁶², Chimera⁶³, and ChimeraX⁶⁴.

Preparation of artificial lipid droplets (ALDs)

The artificial lipid droplets (ALDs) were prepared following a protocol described previously with slight modifications³². Specifically, the 1,2-dioleoyl-sn-glycero-3-phosphocholine (DOPC, Avanti, CAS: 4235-95-4) and 1,2-dioleoyl-sn-glycero-3-phosphoethanolamine (DOPE, Avanti, CAS: 4004-05-1) were dissolved in chloroform. Then the chloroform was evaporated under a nitrogen gas stream. 2 mg of the dried lipids (100% DOPC, or 75%DOPC + 25%DOPE) were resuspended in the lipid droplet buffer (25 mM HEPES pH 7.4, 150 mM NaCl) and then mixed with 5 mg of glyceryl trioleate (Sigma, T7140, CAS: 122-32-7). The mixture was vortexed for 60 cycles of 10 s on and 10 s off. The concentration of ALDs was determined by absorbance at 600 nm.

Flotation assay

The flotation assay was done by following a protocol described previously³¹. Specifically, 15 μg or 30 μg of each protein was incubated at room temperature for 1 h with ALDs (OD₆₀₀ = 2) in 210 μL of an assay buffer containing 25 mM HEPES pH 7.4 and 150 mM NaCl. Then 140 μL of 75% sucrose in the assay buffer was added to give a final sucrose concentration of 30%. To prepare the sucrose density gradient, firstly, 60 μL of the assay buffer was added to the bottom of a new 1.5 mL microtube; secondly, 260 μL of 25% sucrose in the assay buffer was carefully loaded at the bottom of the tube using the pipette; thirdly, 320 μL of the protein-ALDs mixture in 30% sucrose solution was loaded at the bottom of the tube. The tube was centrifuged at 21,100 $\times g$ for 99 min at 23 °C. After centrifugation, three fractions (bottom: 280 μL ; middle: 260 μL ; top: 100 μL) were collected from the bottom to top.

The same volume of each fraction was then analyzed by SDS-PAGE followed by Coomassie blue staining. The intensities of the protein bands on the SDS-PAGE gels were quantified by ImageJ. The binding ratio of each protein with ALDs was calculated using the following equation:

$$\text{Binding ratio (\%)} = D_T \times 100 / (D_T \times 100 + D_M \times 260 + D_B \times 280) \times 100\%$$

in which D_T , D_M , and D_B represent the intensities of HSL from the top (100 μL), middle (260 μL), and bottom (280 μL) fractions on the SDS-PAGE gels, respectively.

Generation of stably transduced Huh-7 cells

To generate the lentivirus, 10 mL of the HEK293T cells (3×10^5 cells/mL) were plated in a 10-cm dish. Once the cells were grown to 60% confluency, they were transfected with 9 μg of pCDH (Addgene plasmid # 72265), 5 μg of pMDL, 3 μg of VSVG and 2 μg of REV plasmids using 38 μg of linear polyethylenimine 25,000 (Polysciences, Cat. No.: 23966). The medium was exchanged 8 h after transfection. The cells were cultured for 48 h after transfection, then the supernatant was harvested and filtered through a 0.22 μm syringe filter. The filtrate containing the virus was used immediately or stored at -80°C .

To generate Huh-7 cells stably expressing EGFP or EGFP fusion proteins, Huh-7 cells seeded on 6-well plates (Corning, Cat. No.: 3516) at 40–60% confluency were infected with a mixture of 1 mL/well of DMEM medium supplemented with 10% FBS and 16 μg of polybrene (Merck, Cat. No.: TR-1003-G) and 1 mL/well of the virus. After 24 h, the medium was replaced with fresh DMEM medium supplemented with 10% (*v/v*) fetal bovine serum (FBS) (Cellmax, SA211.02) and 1% penicillin/streptomycin (P/S) (Cytiva, SV30010). 48 h after infection, the medium was replaced with DMEM medium supplemented with 10% FBS, 1% P/S, and 2 $\mu\text{g}/\text{mL}$ puromycin (invivogen, Cat. No.: ant-pr). The cells were maintained under puromycin selection for 7 days to get the stably transfected Huh-7 cells, passaging as required.

Cell imaging assay

3T3-L1 preadipocytes (ATCC Number: CL_173), HEK293T (ATCC, Cat. No.: CRL-3216), and Huh-7 (Cat. No.: TCHu182) were cultured in the Dulbecco's modified Eagle's medium (DMEM, Gibco, C11995500BT) supplemented with 10% (*v/v*) FBS and 1% P/S at 37°C with 5% CO_2 . Then the cells were seeded to six-well glass bottom plates (NEST, 801004). After 24 h, the confluency reached around 80%. Then the cells were transfected with the plasmids of human HSL and its variants in pcDNA3.1 vector using Lipo3000 (Invitrogen, L3000008). 11 h after transfection, the medium was replaced with fresh DMEM medium supplemented with 10% (*v/v*) FBS, 1% P/S, and 200 μM of oleic acid (aladdin, CAS: 112-80-1) conjugated to fatty acid-free BSA (GOLDBIO, CAS: 9048-46-8) (oleic acid:BSA = 6:1, molar ratio)⁶⁵. The cells were cultured for additional 15 h to enable the formation of lipid droplets. Then the cells were fixed by treating the cells with 4% paraformaldehyde (Beyotime, P0099) for 30 min at room temperature. After fixation, the fixed cells were gently washed with PBS buffer for 3 times to remove residual formaldehyde. Then the neutral lipids in the fixed cells were stained with LipidTOX Deep Red (Invitrogen, HCS LipidTOX™, H34477) at room temperature for at least 30 min before imaging. The cells were imaged with 63 \times oil objectives on a ZEISS LSM 980 in the Airyscan super-resolution mode. The images were processed using the ZEISS ZEN lite software.

For stably transfected Huh-7 cells, the cells at 60% confluency were treated with oleic acid (200 μM) for 15 h to facilitate the formation of lipid droplets. The cells were then fixed with 4% paraformaldehyde and imaged following the protocol detailed above.

To study the effect of PKA activation on HSL localization and phosphorylation, after treating the cells for 15 h with oleic acid conjugated to fatty acid-free BSA, the cells were cultured in DMEM

medium supplemented with 2% fatty acid-free BSA for 1 h. Then the culture medium was replaced by fresh DMEM medium supplemented with 2% fatty acid-free BSA, 1 mM IBMX, and 10 μM forskolin (or the same volume of DMSO), and the cells were cultured for 2 h at 37°C . The cells were then fixed with 4% paraformaldehyde and imaged following the protocol detailed above.

Induced differentiation of 3T3-L1 adipocytes

To generate 3T3-L1 preadipocytes stably expressing EGFP fusion proteins, 3T3-L1 preadipocytes seeded on 6-well plates (Corning, Cat. No.: 3516) at 40–60% confluency were infected with a mixture of 1 mL/well of DMEM medium supplemented with 10% FBS and 16 μg of polybrene (Merck, Cat. No.: TR-1003-G) and 1 mL/well of the lentivirus as mentioned before. After 24 h, the medium was replaced with fresh DMEM medium supplemented with 10% FBS and 1% P/S. After 48 h of infection, the medium was replaced with DMEM medium supplemented with 10% FBS, 1% P/S. Three rounds of lentivirus infections were carried out with HSL-EGFP fusion constructs, passaging as required. The cells were maintained under puromycin selection for 2 rounds to get the stably transfected 3T3-L1 preadipocytes.

The differentiation of 3T3-L1 adipocyte was followed by Abcam's protocol originally adapted from a prior report⁶⁶. Briefly, the stably transfected 3T3-L1 preadipocytes were seeded on six-well plates and in DMEM medium until 70% confluency. 2 days later, the medium was replaced with DMEM supplemented with 10% FBS, 1% P/S, 1 μM dexamethasone (Beyotime, Cat. No.: ST1258), 0.5 mM IBMX (Beyotime, Cat. No.: ST1398), and 10 $\mu\text{g}/\text{mL}$ insulin (Beyotime, Cat. No.: P3376). After 2 days, cells were maintained in DMEM medium containing 10% FBS, 1% P/S, 10 $\mu\text{g}/\text{mL}$ insulin for 2 days, then in DMEM medium containing 10% FBS, 1% P/S, without insulin for an additional 3–4 days before use. To study the effect of PKA activation on HSL localization and phosphorylation, the cells were cultured in DMEM medium supplemented with 2% fatty acid-free BSA, 1 mM IBMX, and 10 μM forskolin (or the same volume of DMSO), and the cells were cultured for 2 h at 37°C . The cells were then measured for the phosphorylation level by Western blot or fixed with 4% paraformaldehyde and imaged with 63 \times oil objectives on a ZEISS LSM 980 confocal microscope.

Reverse transcription and qPCR analysis

The total RNA of 3T3-L1 preadipocytes, 3T3-L1 preadipocytes treated with OA, and 3T3-L1 adipocytes was extracted with TRIzol reagent (Invitrogen). 1 μg of the total RNA was reversely transcribed into cDNA using HiScript II 1st Strand cDNA Synthesis Kit (Vazyme). The cDNA was then used as the template for qPCR analysis using Hieff qPCR SYBR Green Master Mix (YEASEN) on the CFX Connect Real-Time PCR Detection System (Bio-Rad). The mRNA expression levels were normalized to β -actin. The qPCR primers used in this study are listed as follows:

PLIN1:

Forward sequence (5'–3'): GGGACCTGTGAGTGCTTCC

Reverse sequence (5'–3'): GTATTGAAGAGCCGGGATCTTTT

β -actin:

Forward sequence (5'–3'): GGCTGTATTCCCTCCATCG

Reverse sequence (5'–3'): CCAGTTGGTAACAATGCCATGT

Image quantification and statistics

The LD-targeted signal was calculated and analyzed following a protocol described previously⁶⁷. Specifically, ImageJ software was used to analyze all the images⁶⁸. To determine the LD area in the cell, Otsu thresholding was applied to the LipidTOX channel, and the resulting area was measured. The image was background-corrected, and the mean EGFP signal in that region was quantified. Then, the size and the mean EGFP signal of the whole cell were measured. To quantify the %LD-targeted signal for different HSL-EGFP constructs, the total EGFP signal on LDs was calculated as a ratio to the total

EGFP signal in the entire cell. The results represented the mean \pm SD of three independent experiments ($n=15$, a total of 15 cells were analyzed from three independent measurements) and were analyzed using the unpaired t -test in Prism to calculate the two-tailed P -values.

Detection of the phosphorylation level of HSL that was transiently expressed in cells

After the cells were treated with 1 mM IBMX, and 10 μ M forskolin (or the same volume of DMSO), they were collected and washed once with 1 \times PBS and then lysed with 100 μ L of RIPA buffer (Beyotime #P0013B) supplemented with a protease inhibitor cocktail (VWR International). The concentration of each sample was determined by BCA assay (Thermo Fisher Scientific, Cat. No.: 23225 and Cat. No.: 23227). Equal amounts of each sample were mixed with 5 \times SDS Loading buffer and boiled at 98 $^{\circ}$ C for 5 min. The samples were subjected to SDS-PAGE and then transferred to a 0.22 μ m polyvinylidene fluoride membrane. After blocking with 5% milk, the membrane was probed with the primary antibodies, including anti-FLAG (Sigma-Aldrich, F1804), anti-GFP (Proteintech, HRP-66002), anti-PLIN1-pS522 (Vala Sciences, 4856), anti-HSL-pS660 (CST, 45804S), anti-HSL-pS565 (CST, 4137T), anti-GAPDH (immunoWay, YM3029), anti- β -actin (immunoWay, YM3028), and the secondary antibodies including goat anti-rabbit IgG horseradish peroxidase (Sigma #API56P) and goat anti-mouse IgG horseradish peroxidase (Sigma #API57P) at a dilution ratio of 1:10,000 in TBST buffer. The chemiluminescence signal of the horseradish peroxidase was detected using Amersham Imager 680 (Cytiva).

Phosphorylation and dephosphorylation of purified HSL and PLIN1

Purified HSL (final concentration: 17.5 μ M) was phosphorylated by PKA (final concentration: 5.7 μ M) in 1 mL of a phosphorylation buffer (25 mM Tris-HCl pH 8.0, 150 mM NaCl, 0.01% GDN, 10 mM DTT, 50 mM MgCl₂, 10 mM ATP) for 2 h at 4 $^{\circ}$ C. Then HSL in the sample was purified by gel filtration (Superdex 200 increase, 10/30, GE Healthcare) with a running buffer containing 25 mM Tris-HCl pH 8.0, 150 mM NaCl, and 0.01% GDN. The peak fractions were collected and used for biochemical assays. Purified HSL was dephosphorylated by incubating HSL (final concentration: 17.5 μ M) with PP1 α (final concentration: 2.5 μ M) in 1 mL of a dephosphorylation buffer (25 mM Tris-HCl pH 8.0, 150 mM NaCl, 0.01% GDN, 5 mM MnCl₂) for 2 h at 4 $^{\circ}$ C. Then HSL in the sample was purified by gel filtration (Superdex 200 increase, 10/30, GE Healthcare). After phosphorylation or dephosphorylation, the HSL samples were analyzed by Western Blot. After phosphorylation or dephosphorylation, the HSL samples were analyzed by mass spectrometry and Western blot. The phosphorylation or dephosphorylation of purified PLIN1 was performed using the same protocol as HSL.

Reporting summary

Further information on research design is available in the Nature Portfolio Reporting Summary linked to this article.

Data availability

The cryo-EM structure of human HSL has been deposited in the Protein Data Bank (www.rcsb.org) with the accession code [8ZVQ](#). The cryo-EM map has been deposited in the Electron Microscopy Data Bank with the accession code [EMD-60512](#). All other data are available in the manuscript or the supplementary materials. The crystal structure of the carboxylesterase EST2 ([PDB: 1QZ3](#)) was used for structural analysis in this study. Mass spectrometry proteomics data are available in PRIDE with the dataset identifier [PXD062014](#). Source data are provided with this paper.

References

- Pol, A., Gross, S. P. & Parton, R. G. Review: biogenesis of the multifunctional lipid droplet: lipids, proteins, and sites. *J. Cell Biol.* **204**, 635–646 (2014).
- Olzmann, J. A. & Carvalho, P. Dynamics and functions of lipid droplets. *Nat. Rev. Mol. Cell Biol.* **20**, 137–155 (2019).
- Lass, A., Zimmermann, R., Oberer, M. & Zechner, R. Lipolysis - a highly regulated multi-enzyme complex mediates the catabolism of cellular fat stores. *Prog. Lipid Res.* **50**, 14–27 (2011).
- Vaughan, M., Berger, J. E. & Steinberg, D. Hormone-Sensitive Lipase and Monoglyceride Lipase Activities in Adipose Tissue. *J. Biol. Chem.* **239**, 401–409 (1964).
- Walsh, D. A., Perkins, J. P. & Krebs, E. G. An adenosine 3',5'-monophosphate-dependant protein kinase from rabbit skeletal muscle. *J. Biol. Chem.* **243**, 3763–3765 (1968).
- De Lean, A., Stadel, J. M. & Lefkowitz, R. J. A ternary complex model explains the agonist-specific binding properties of the adenylate cyclase-coupled beta-adrenergic receptor. *J. Biol. Chem.* **255**, 7108–7117 (1980).
- Northup, J. K. et al. Purification of the regulatory component of adenylate cyclase. *Proc. Natl Acad. Sci. USA* **77**, 6516–6520 (1980).
- Cerione, R. A. et al. The mammalian beta 2-adrenergic receptor: reconstitution of functional interactions between pure receptor and pure stimulatory nucleotide binding protein of the adenylate cyclase system. *Biochemistry* **23**, 4519–4525 (1984).
- Smigel, M. D. Purification of the catalyst of adenylate cyclase. *J. Biol. Chem.* **261**, 1976–1982 (1986).
- Stralfors, P., Bjorgell, P. & Belfrage, P. Hormonal regulation of hormone-sensitive lipase in intact adipocytes: identification of phosphorylated sites and effects on the phosphorylation by lipolytic hormones and insulin. *Proc. Natl Acad. Sci. USA* **81**, 3317–3321 (1984).
- Anthonsen, M. W., Ronnstrand, L., Wernstedt, C., Degerman, E. & Holm, C. Identification of novel phosphorylation sites in hormone-sensitive lipase that are phosphorylated in response to isoproterenol and govern activation properties in vitro. *J. Biol. Chem.* **273**, 215–221 (1998).
- Su, C. L. et al. Mutational analysis of the hormone-sensitive lipase translocation reaction in adipocytes. *J. Biol. Chem.* **278**, 43615–43619 (2003).
- Krintel, C. et al. Ser649 and Ser650 are the major determinants of protein kinase A-mediated activation of human hormone-sensitive lipase against lipid substrates. *PLoS ONE* **3**, e3756 (2008).
- Krintel, C., Morgelin, M., Logan, D. T. & Holm, C. Phosphorylation of hormone-sensitive lipase by protein kinase A in vitro promotes an increase in its hydrophobic surface area. *FEBS J.* **276**, 4752–4762 (2009).
- Miyoshi, H. et al. Perilipin promotes hormone-sensitive lipase-mediated adipocyte lipolysis via phosphorylation-dependent and -independent mechanisms. *J. Biol. Chem.* **281**, 15837–15844 (2006).
- Miyoshi, H. et al. Control of adipose triglyceride lipase action by serine 517 of perilipin A globally regulates protein kinase A-stimulated lipolysis in adipocytes. *J. Biol. Chem.* **282**, 996–1002 (2007).
- Granneman, J. G., Moore, H. P., Krishnamoorthy, R. & Rathod, M. Perilipin controls lipolysis by regulating the interactions of AB-hydrolase containing 5 (Abhd5) and adipose triglyceride lipase (Atgl). *J. Biol. Chem.* **284**, 34538–34544 (2009).
- Keenan, S. N. et al. Perilipin 5 S155 phosphorylation by PKA is required for the control of hepatic lipid metabolism and glycemic control. *J. Lipid Res.* **62**, 100016 (2021).
- Pagnon, J. et al. Identification and functional characterization of protein kinase A phosphorylation sites in the major lipolytic protein, adipose triglyceride lipase. *Endocrinology* **153**, 4278–4289 (2012).

20. Sahu-Osen, A. et al. CGI-58/ABHD5 is phosphorylated on Ser239 by protein kinase A: control of subcellular localization. *J. Lipid Res* **56**, 109–121 (2015).
21. Grisetti, E. et al. Molecular mechanisms of perilipin protein function in lipid droplet metabolism. *FEBS Lett.* **598**, 1170–1198 (2024).
22. Sztalryd, C. et al. Perilipin A is essential for the translocation of hormone-sensitive lipase during lipolytic activation. *J. Cell Biol.* **161**, 1093–1103 (2003).
23. Clifford, G. M., Londos, C., Kraemer, F. B., Vernon, R. G. & Yeaman, S. J. Translocation of hormone-sensitive lipase and perilipin upon lipolytic stimulation of rat adipocytes. *J. Biol. Chem.* **275**, 5011–5015 (2000).
24. Morimoto, C., Kameda, K., Tsujita, T. & Okuda, H. Relationships between lipolysis induced by various lipolytic agents and hormone-sensitive lipase in rat fat cells. *J. Lipid Res.* **42**, 120–127 (2001).
25. Prats, C. et al. Decrease in intramuscular lipid droplets and translocation of HSL in response to muscle contraction and epinephrine. *J. Lipid Res.* **47**, 2392–2399 (2006).
26. Holst, L. S. et al. Molecular cloning, genomic organization, and expression of a testicular isoform of hormone-sensitive lipase. *Genomics* **35**, 441–447 (1996).
27. Mulder, H. et al. Hormone-sensitive lipase, the rate-limiting enzyme in triglyceride hydrolysis, is expressed and active in beta-cells. *Diabetes* **48**, 228–232 (1999).
28. Grober, J. et al. Characterization of the promoter of human adipocyte hormone-sensitive lipase. *Biochem. J.* **328**, 453–461 (1997).
29. Holm, C. et al. Hormone-sensitive lipase: sequence, expression, and chromosomal localization to 19 cent-q13.3. *Science* **241**, 1503–1506 (1988).
30. Ogiyama, T. et al. Design, synthesis, and pharmacological evaluation of a novel series of hormone sensitive lipase inhibitor. *Bioorg. Med. Chem.* **25**, 4817–4828 (2017).
31. Rowe, E. R. et al. Conserved amphipathic helices mediate lipid droplet targeting of perilipins 1–3. *J. Biol. Chem.* **291**, 6664–6678 (2016).
32. Wang, Y. et al. Construction of nanodroplet/adiposome and artificial lipid droplets. *ACS Nano* **10**, 3312–3322 (2016).
33. Zhi, Z. et al. Protocol for using artificial lipid droplets to study the binding affinity of lipid droplet-associated proteins. *STAR Protoc.* **3**, 101214 (2022).
34. Bartz, R. et al. Lipidomics reveals that adiposomes store ether lipids and mediate phospholipid traffic. *J. Lipid Res.* **48**, 837–847 (2007).
35. Holm, C., Fredrikson, G., Sundler, R. & Belfrage, P. Incorporation of hormone-sensitive lipase into phosphatidylcholine vesicles. *Lipids* **25**, 254–259 (1990).
36. Ogiyama, T. et al. Identification of a novel hormone sensitive lipase inhibitor with a reduced potential of reactive metabolites formation. *Bioorg. Med. Chem.* **25**, 2234–2243 (2017).
37. Wei, Y. et al. Crystal structure of brefeldin A esterase, a bacterial homolog of the mammalian hormone-sensitive lipase. *Nat. Struct. Biol.* **6**, 340–345 (1999).
38. De Simone, G. et al. A snapshot of a transition state analogue of a novel thermophilic esterase belonging to the subfamily of mammalian hormone-sensitive lipase. *J. Mol. Biol.* **303**, 761–771 (2000).
39. De Simone, G. et al. A substrate-induced switch in the reaction mechanism of a thermophilic esterase: kinetic evidences and structural basis. *J. Biol. Chem.* **279**, 6815–6823 (2004).
40. Palm, G. J. et al. The crystal structure of an esterase from the hyperthermophilic microorganism *Pyrobaculum calidifontis* VA1 explains its enantioselectivity. *Appl. Microbiol. Biotechnol.* **91**, 1061–1072 (2011).
41. Kim, S. H., Kang, P. A., Han, K., Lee, S. W. & Rhee, S. Crystal structure of chloramphenicol-metabolizing enzyme EstDL136 from a metagenome. *PLoS ONE* **14**, e0210298 (2019).
42. Dufau, J. et al. In vitro and ex vivo models of adipocytes. *Am. J. Physiol. Cell Physiol.* **320**, C822–C841 (2021).
43. Granneman, J. G., Moore, H. H., Mottillo, E. P. & Zhu, Z. Functional interactions between Mldp (LSDP5) and Abhd5 in the control of intracellular lipid accumulation. *J. Biol. Chem.* **284**, 3049–3057 (2009).
44. Gunn, P. J., Green, C. J., Pramfalk, C. & Hodson, L. In vitro cellular models of human hepatic fatty acid metabolism: differences between Huh7 and HepG2 cell lines in human and fetal bovine culturing serum. *Physiol. Rep.* **5**, e13532 (2017).
45. Konermann, L., Pan, J. & Liu, Y. H. Hydrogen exchange mass spectrometry for studying protein structure and dynamics. *Chem. Soc. Rev.* **40**, 1224–1234 (2011).
46. Choi, Y. M. et al. Structural insights into perilipin 3 membrane association in response to diacylglycerol accumulation. *Nat. Commun.* **14**, 3204 (2023).
47. Jumper, J. et al. Highly accurate protein structure prediction with AlphaFold. *Nature* **596**, 583–589 (2021).
48. Garton, A. J. & Yeaman, S. J. Identification and role of the basal phosphorylation site on hormone-sensitive lipase. *Eur. J. Biochem.* **191**, 245–250 (1990).
49. Zhang, H. et al. Bright and stable monomeric green fluorescent protein derived from StayGold. *Nat. Methods* **21**, 657–665 (2024).
50. Greenberg, A. S. et al. Perilipin, a major hormonally regulated adipocyte-specific phosphoprotein associated with the periphery of lipid storage droplets. *J. Biol. Chem.* **266**, 11341–11346 (1991).
51. Granneman, J. G. et al. Analysis of lipolytic protein trafficking and interactions in adipocytes. *J. Biol. Chem.* **282**, 5726–5735 (2007).
52. Zhang, C. & Liu, P. The new face of the lipid droplet: lipid droplet proteins. *Proteomics* **19**, e1700223 (2019).
53. Dhiman, R. et al. Hairpin protein partitioning from the ER to lipid droplets involves major structural rearrangements. *Nat. Commun.* **15**, 4504 (2024).
54. Shen, W. J., Patel, S., Hong, R. & Kraemer, F. B. Hormone-sensitive lipase functions as an oligomer. *Biochemistry* **39**, 2392–2398 (2000).
55. Krintel, C., Klint, C., Lindvall, H., Morgelin, M. & Holm, C. Quaternary structure and enzymological properties of the different hormone-sensitive lipase (HSL) isoforms. *PLoS One* **5**, e11193 (2010).
56. Masson, G. R. et al. Recommendations for performing, interpreting and reporting hydrogen deuterium exchange mass spectrometry (HDX-MS) experiments. *Nat. Methods* **16**, 595–602 (2019).
57. Basu, D., Manjur, J. & Jin, W. Determination of lipoprotein lipase activity using a novel fluorescent lipase assay. *J. Lipid Res.* **52**, 826–832 (2011).
58. Punjani, A., Rubinstein, J. L., Fleet, D. J. & Brubaker, M. A. cryoSPARC: algorithms for rapid unsupervised cryo-EM structure determination. *Nat. Methods* **14**, 290–296 (2017).
59. Wang, N. et al. Structural basis of human monocarboxylate transporter 1 inhibition by anti-cancer drug candidates. *Cell* **184**, 370–383 e313 (2021).
60. Emsley, P. & Cowtan, K. Coot: model-building tools for molecular graphics. *Acta Crystallogr. D. Biol. Crystallogr.* **60**, 2126–2132 (2004).
61. Adams, P. D. et al. PHENIX: a comprehensive Python-based system for macromolecular structure solution. *Acta Crystallogr. D. Biol. Crystallogr.* **66**, 213–221 (2010).
62. Schrodinger, LLC. *The PyMOL Molecular Graphics System, Version 1.8* (2015).
63. Pettersen, E. F. et al. UCSF Chimera—a visualization system for exploratory research and analysis. *J. Comput. Chem.* **25**, 1605–1612 (2004).
64. Goddard, T. D. et al. UCSF ChimeraX: Meeting modern challenges in visualization and analysis. *Protein Sci.* **27**, 14–25 (2018).

65. Bosch, M. et al. Mammalian lipid droplets are innate immune hubs integrating cell metabolism and host defense. *Science* **370**, eaay8085 (2020).
66. Reed, B. C. & Lane, M. D. Insulin receptor synthesis and turnover in differentiating 3T3-L1 preadipocytes. *Proc. Natl Acad. Sci. USA* **77**, 285–289 (1980).
67. Kory, N., Thiam, A. R., Farese, R. V. Jr & Walther, T. C. Protein crowding is a determinant of lipid droplet protein composition. *Dev. Cell* **34**, 351–363 (2015).
68. Schneider, C. A., Rasband, W. S. & Eliceiri, K. W. NIH Image to ImageJ: 25 years of image analysis. *Nat. Methods* **9**, 671–675 (2012).

Acknowledgements

We would like to thank Prof. Yigong Shi for discussion. We would like to thank Drs. Dante Neculai and Xudong Wu for valuable comments. We would like to thank the Cryo-EM Facility and High-Performance Computing Center of Westlake University for providing cryo-EM and computation support, the staff at the Westlake University Microscopy Core Facility for advice and assistance in light microscopy sample preparation and data collection, the Mass Spectrometry & Metabolomics Core Facility at the Center for Biomedical Research Core Facilities of Westlake University for sample analysis. This work was supported by Westlake Laboratory of Life Sciences and Biomedicine, Westlake Education Foundation, and “Pioneer” and “Leading Goose” R&D Program of Zhejiang (2024SSYS0036) to Q.H.; National Natural Science Foundation of China (32271261), Zhejiang Provincial Natural Science Foundation of China (LR22C050003 and LDG25C050002), Westlake University (1011103860222B1) and Westlake Education Foundation (101486021901) to J.W.

Author contributions

Q.H. conceived and supervised the project; H.P. purified the proteins, performed the biochemical assays and cell imaging assays, prepared the cryo-EM samples, and collected the cryo-EM data; T.Z. purified the proteins, performed the biochemical assays and cell imaging assays; J.Z. contributed to cell imaging; X.G. contributed to protein purification and performed biochemical assays; Q.X. and J.W. calculated the cryo-EM map and built the model; J.P. and S.F. performed the HDX-MS experiment; all authors contributed to data analysis; Q.H. and H.P. wrote the manuscript with inputs from other authors.

Competing interests

The authors declare no competing interests.

Additional information

Supplementary information The online version contains supplementary material available at <https://doi.org/10.1038/s41467-025-58887-z>.

Correspondence and requests for materials should be addressed to Jianping Wu or Qi Hu.

Peer review information *Nature Communications* thanks Michael Airola, Siavash Vahidi and the other, anonymous, reviewer(s) for their contribution to the peer review of this work. A peer review file is available.

Reprints and permissions information is available at <http://www.nature.com/reprints>

Publisher's note Springer Nature remains neutral with regard to jurisdictional claims in published maps and institutional affiliations.

Open Access This article is licensed under a Creative Commons Attribution-NonCommercial-NoDerivatives 4.0 International License, which permits any non-commercial use, sharing, distribution and reproduction in any medium or format, as long as you give appropriate credit to the original author(s) and the source, provide a link to the Creative Commons licence, and indicate if you modified the licensed material. You do not have permission under this licence to share adapted material derived from this article or parts of it. The images or other third party material in this article are included in the article's Creative Commons licence, unless indicated otherwise in a credit line to the material. If material is not included in the article's Creative Commons licence and your intended use is not permitted by statutory regulation or exceeds the permitted use, you will need to obtain permission directly from the copyright holder. To view a copy of this licence, visit <http://creativecommons.org/licenses/by-nc-nd/4.0/>.

© The Author(s) 2025